Molecules in Sculpted Fields: Magnetic Field Effects and Multipole Transitions

Molecules in sculpted fields: magnetic field effects and multipole transitions

A dissertation presented

by

Nan Yang

to

The School of Engineering and Applied Sciences

in partial fulfillment of
the requirements for the degree of
Doctor of Philosophy
in the subject of
Applied Physics

Harvard University

Cambridge, Massachusetts

December 2012

Prof. Adam Cohen Nan Yang

Molecules in sculpted fields: magnetic field effects and multipole transitions

Abstract

This thesis describes work related to the theme of sculpted electromagnetic fields - engineered fields with particular spatial patterns - and their interactions with molecules. We are motivated by the following questions: what are ways of detecting spatial patterns in electromagnetic fields? What are possible applications of spatially engineered fields? Are there molecular transitions that are dark to plane waves but that can be probed by sculpted fields?

The first part of this thesis is in the area of magnetic field effects in chemistry. We focus on magnetic field modulated fluorescence, which provides a convenient method for imaging magnetic field strength. We proposed and demonstrated a fluorescence technique that allows imaging through strongly scattering media. We achieve this by exploiting the fact that most materials do not scatter magnetic field. This allows us to project a magnetic field pattern beyond the scattering surface. The magnetic field dependent fluorescence then allows us to map out the object of interest. We constructed a setup that demonstrates 2D imaging using this technique. We synthesized new molecular systems to enhance the sensitivity to magnetic field. We characterized and compared these molecules with steady state fluorescence spectroscopy, transient

fluorescence and transient absorption measurements. The results reveal patterns that point to directions for engineering chemical systems to further enhance their magnetic field sensing properties.

The second portion of this thesis is a theoretical study of the molecular multipole transitions and their couplings to local electromagnetic quantities. Using a semiclassical approach, we performed a multipole expansion of molecular transitions driven by monochromatic radiation. We derived the local electromagnetic quantities that couple to different multipole transitions and observables such as circular dichroism and magnetic circular dichroism. It was observed that certain transitions are dark to plane waves, but could be probed by simple spatial arrangements such as superpositions of plane waves. Experiments for their detection are also proposed.

Contents

List of Tables

List of Figures

Acknowledgements

I am grateful for the opportunity to work in Adam's lab. Observing and participating in the growth of a new research lab is truly a unique experience. In addition to being a bright and dedicated scientist, Adam has also been an inspiring advisor. For all of these I am truly grateful, and in particular the marvelous opportunity to see how hard work and careful reasoning can turn an idea or even just a hunch into a discovery. Of course, things do not always go smoothly and sometimes there have been setbacks and detours as in all non-trivial endeavors. I have learned an incredible amount from the entire experience and that will always be with me.

Over the course of my PhD, I have met and worked with many smart and friendly colleagues in our lab. I thank Hohjai Lee, Prashant Jain, Rohini Shivamoggi, and Vijay Jain, who have at various times worked with me on the same or related projects. I also would like to thank my lab mates: Alex Fields, Jennifer Hou, Yiqiao Tang, Halil Bayraktar, Min Ju Shon, Joel Kralj, Sabrina Leslie, Daniel Hochbaum, Veena Venkatachalam, Dougal MacLaurin, Jeehae Park, Dian Yang, Kit Werley and Daan Brinks. The presence of these wonderful colleagues has made life in the lab much more enjoyable, and I have learned a lot from all of them.

I have also received valuable help from many people outside of our lab. I thank Michael Campbell and Prof. Tobias Ritter for teaching me basic organic synthesis from scratch, as well as providing suggestions and apparatus that are crucial for the project. I thank Ryan Spoering for discussions on the reaction scheme. I have had the chance to

work with Matt Rosen and Brandon Armstrong at the Martinos center for biomedical imaging. I am very grateful for their effort in construction of a setup for performing ESR experiments with our samples. It was a great pleasure to work there and I learned a lot from their expertise. I have spent a significant portion of my time working at the facilities of the Center for Nanoscale Systems (CNS), and the magnetic resonance facility at the department of chemistry and chemical biology. I thank the staff for their help and kindness.

I thank my committee members for helpful discussions and feedback: Adam, L. Mahadevan, Ronald Walsworth, and Navin Khaneja. I am particularly grateful for their kindness and encouragement.

Our projects are supported by funding from the Office of Naval Research (ONR), the Defense Advanced Research Projects Agency (DARPA), and Presidential Early Career Award for Scientists and Engineers (PECASE). I thank Natural Sciences and Engineering Research Council (NSERC) of Canada for funding my PGS D scholarship.

Finally, I thank my parents, whose support has meant a lot to me every step of the way. I have always treasured the opportunity to pursue a PhD, partly because I know it is an opportunity that was not available to them.

Introduction

One of the principle research interests of our lab is to study the interactions of molecules with sculpted electromagnetic (EM) fields [1]. By sculpted fields we mean EM fields with engineered spatial patterns that are not found in plane waves or uniform DC fields, as are employed in common spectroscopic methods. As developments in ultrafast techniques continue to push temporal control of EM fields into new frontiers, spatially engineered fields provide important complementary information. Eventually, spatial and temporal sculpting are both required to achieve the ultimate goal of complete control of electromagnetic fields. During my PhD, I worked on two areas related to the theme of engineered EM fields: magnetic field effect on chemistry and molecular multipole transitions.

Chapter 1 provides the background information of magnetic field effect (MFE) on chemistry, relevant works from literature, and the basic underlying mechanism. Chapter 2 presents basic MFE measurements that we performed to characterize the intermolecular electron transfer systems. Chapter 3 describes a potential application of MFE that we have proposed and demonstrated. It is a technique for imaging through strongly scattering media using the chemical system mentioned in Chapter 2. Chapter 4 describes our effort on improving the chemical system by covalently linking the electron transfer partners. Thereby create a system that experience intramolecular rather than intermolecular electron transfer. This significantly enhanced the properties of the system with respect to MFE. Chapter 5 presents characterization and comparison of the molecules that we synthesized. The patterns revealed point to potential directions for engineering

magnetically sensitive chemical systems to enhance their properties. Chapter 6 discusses the local geometry of electromagnetic fields and its role in molecular multipole transitions. We derive the local EM quantities that couple to different multipole transitions and other observables such as circular dichroism and magnetic circular dichroism. We show that some of these transitions do not interact with plane waves, but could be probed by simple spatial arrangements such as superpositions of plane waves. Experiments for their detection are also proposed. Below is a list of publications related to my work described in this thesis:

Yang, N., Tang, Y. & Cohen, A. E. Spectroscopy in sculpted fields. *Nano Today* **4**, 269-279 (2009).

Yang, N. & Cohen, A. E. Optical imaging through scattering media via magnetically modulated fluorescence. *Opt. Express* **18**, 25461 (2010).

Yang, N. Y. & Cohen, A. E. Local geometry of electromagnetic fields and its role in molecular multipole transitions. *J. Phys. Chem. B* **115**, 5304-5311 (2011).

Lee, H., Yang, N. & Cohen, A. E. Mapping nanomagnetic fields using a radical pair reaction. *Nano Lett.* **11**, 5367-5372 (2011).

Chapter 1 Background and Theory

1.1 Magnetic field effects on chemical reactions

The effects of magnetic fields on chemical reactions are well documented with experimental observations in many different systems[2-5]. The area has attracted significant research effort over the past few decades, yet still contains many interesting, unexplored territories. It was initially surprising that ordinary magnetic fields (<1 T) would have any effects on chemical processes. Early theoretical argument based on thermodynamics suggested that the rate of chemical reactions involving paramagnetic states would be affected by magnetic fields. However, the interaction energy of an electron spin with a relatively large external field of 1 T is about 60 μeV, compared to thermal energy of 25 meV at room temperature. Therefore, without going to low temperature, magnetic effects on thermoequilibrium and reaction rates are negligible even at high fields.

The discovery of the radical pair mechanism (RPM) in the late 1960's proved to be a successful theory for explaining the many experiment observations of magnetic field effects (MFE) in chemistry. The theory made the crucial connection between electron spin and chemical pathways via the Pauli exclusion principle. External magnetic fields affect the evolution of the spin states, which subsequently determine the chemical pathways available to the system. In section 1.2, we will examine the RPM in detail as it is applied to the chemical systems investigated in this thesis.

1.2 The radical pair mechanism

The radical pair mechanism was independently proposed by Kaptein and Oosterhoff[6,7] and by Closs[8] in 1969. We present the theory as it is applied to electron transfer systems, as those are what I have studied experimentally.

Let us first consider the energy diagram of a single molecule as shown in Fig. 1.1.

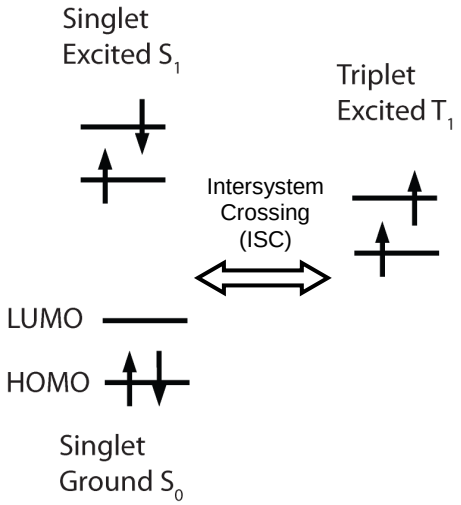

Fig. 1.1 The relevant states in molecular photochemistry

The lower and upper bars represent the highest occupied molecular orbital (HOMO) and lowest unoccupied molecular orbital (LUMO), respectively. The arrows indicate electrons that are initially at the HOMO. The up and down direction of the arrows symbolize electron spins. For a pair of electrons, arrows in the opposite direction symbolize a singlet state, and arrows in the same direction symbolize a triplet state. By Pauli exclusion principle, electrons at the same orbital must be in the singlet state. The molecule is usually in its electronic ground states S_0, as shown at the bottom of the figure. When the molecule is excited by absorbing a photon, one electron goes into a higher energy level. Spin-flipping transitions are forbidden due to selection rules, therefore the

spin configuration is preserved and remains singlet. So we have a singlet excited state S_1 at a higher energy to S_0. Magnetic interactions can flip or rephase the electron spins and lead to interconversion between the singlet excited and triplet excited state T_1. The interconversion is referred to as intersystem crossing (ISC). Electrons are fermions, so their overall wave function is antisymmetric. The overall wave function is a direct product of the spin wave function and the spatial wave function. Singlet and triplet states have antisymmetric and symmetric spin wave functions, respectively. Therefore they have symmetric and antisymmetric spatial wave functions, respectively. Antisymmetric spatial wave function means that the two electrons have zero probability density to have the same spatial coordinates. Therefore the Coulomb energy is lower for the triplet states, as indicated by the level of the T_1 in Fig. 1.1. This is the exchange interaction and can be in general written as:

$$H_J = J(\mathrm{S}_1 \cdot \mathrm{S}_2). \tag{1.1}$$

The eigenstates of ($\mathbf{S}_1 \cdot \mathbf{S}_2$) are singlet and triplet states. Now we consider two molecules, a system consisting of an electron donor and acceptor. The Hamiltonian is

$$\begin{aligned} H &= H_J + H_B + H_{hf} \\ &= J(\mathrm{S}_1 \cdot \mathrm{S}_2) + B(g_1 S_{1z} + g_2 S_{2z}) + \sum_{i=1}^{N_1} A_i I_i \cdot \mathrm{S}_1 + \sum_{k=1}^{N_{21}} A_k I_k \cdot \mathrm{S}_2 \end{aligned}. \tag{1.2}$$

The terms in the Hamiltonian are: H_J is the exchange interaction, H_B is the Zeeman interaction with the external field, and H_{hf} is the hyperfine interaction between the electron spin and nuclear spins.

When the distance separating the radical pair is small, H_J dominates, and the splitting between singlet and triplet states prevents any intersystem crossing. If the radicals move away from each other by diffusion or other process, then H_J decreases rapidly with distance, and becomes negligible when the radicals are sufficiently far apart (>1 nm). It is also worth noting that spin-orbit interactions, while responsible for intersystem crossing in molecules in excited states, are similarly negligible at large radical separation[9].

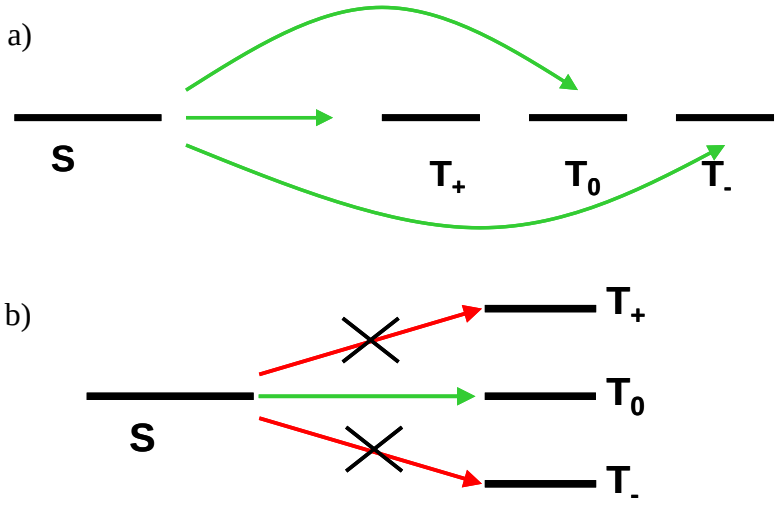

Fig. 1.2 a) Intersystem crossing in absence of external field b) intersystem crossing in presence of external field

When the radical pair is well-separated, singlet and triplet states become degenerate. The electron spins experience different local hyperfine fields from magnetically active nuclei such as ^{1}H, ^{13}C, ^{14}N. The difference in x and y components of the local hyperfine fields lead to spin flipping and intersystem crossing between S_0 and $T_{\pm 1.}$ Difference in z components leads to rephasing and intersystem crossing between S_0

and T_0. The system starts in the singlet state and ISC to the three triplet states are equally efficient as all states are degenerate, as shown in Fig. 1.2a.

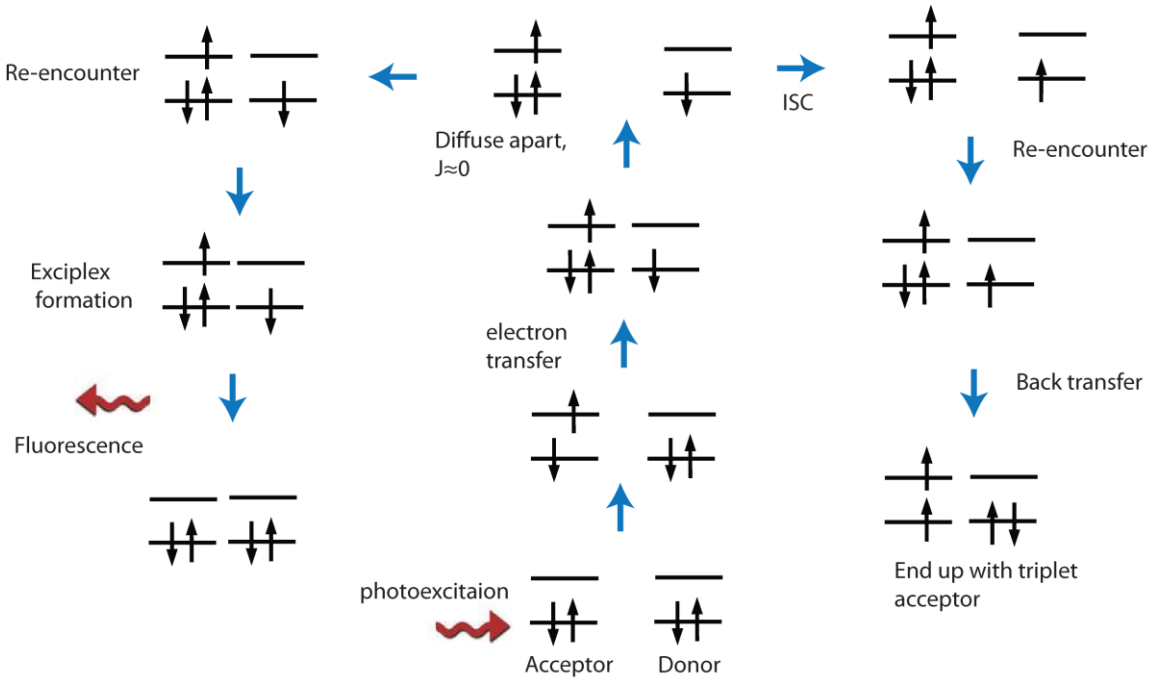

Fig. 1.3 The evolution of radical pairs created by photo-initiated electron transfer, the applied field affects the ISC step

Now consider the effect of applied external field through the Zeeman term. In general the g factors of the electrons could be different, but the difference is usually small and can be neglected when field is low. As shown in Fig. 1.2b. Now the degeneracy of the states is lifted, with $T_{\pm1}$ split away. ISC to the $T_{\pm1}$ states is effectively suppressed when the splitting is greater than the difference in hyperfine fields experienced by the two electrons. The hyperfine field is typically of the order of 10 G. Although this is still large compared to the Earth's magnetic field of about 0.5 G, it is sufficiently low to be easily

arranged via electromagnet or permanent magnets. This is why relatively weak magnetic fields can influence chemical processes: the field does not have to compete with thermal energy, but only with the hyperfine field.

The process as applied to an electron transfer system is illustrated in Fig. 1.3. Photoexcitation of the acceptor promotes one electron to the higher energy level. When the donor and the excited acceptor are in proximity of each other, an electron transfer from the donor to the acceptor can take place. This creates a pair of charged radicals, and the spin of this radical pair is initially in the singlet state. When the donor and acceptor diffuse apart from each other so that the exchange integral J becomes negligible, hyperfine interaction dominates and induces ISC. Then there are two pathways. If ISC does not occur, then the system remains in the singlet state, and upon reencountering, the system can form an excited complex or exciplex[10]. The exciplex can decay radiatively to the singlet ground state and give off fluorescence, which is the signal we detect in many of our experiments.

The system could also undergo ISC, so a triplet radical pair is formed. At reencountering, Pauli exclusion principle forbids relaxation back to the ground state, so no fluorescence is produced. Often there is an electron back transfer to the acceptor, creating triplet acceptor species. The triplet species can decay non-radiatively or go through triplet-triplet annihilation when two of the molecules encounter, and give off delayed fluorescence [11]. The intensity of the delayed fluorescence is much weaker compared to the direct exciplex fluorescence for dilute solutions, as its intensity is proportion to the concentration squared.

Consider the experiment of measuring the fluorescence intensity as a function of applied magnetic field. We would observe an increase of fluorescence with increasing field strength, because magnetic field suppresses ISC, so the radical pair is more likely to be in the singlet state and form exciplex which then decays radiatively. This is the most common mechanism for MFE when the field is not very strong (< 1 T). It is referred to as the hyperfine mechanism, as the external field is competing against the nuclear hyperfine fields and suppressing the hyperfine fields' ability to induce ISC.

For samples that do not have nuclear polarization or particular molecular orientation, the MFE only depends on the magnitude of the magnetic field, and not on the direction. This means that the effect on unoriented molecules cannot function as a compass. We will discuss more about this in section 1.4 in relation to hypothesis of magnetocompass in organisms.

We should note that ISC is not a one-way conversion from the singlet to the triplet state. Rather, it is an interconversion process with triplet states also going into the singlet state. Since the nuclear spin relaxation is generally much slower than the electronic processes, we assume the hyperfine field is constant on the time scale of interest. Then the long-time steady state singlet ratios are 1/3 and 1/2 in the no field and high field limits, respectively. The result in the no field limit may seem surprising given that there are three triplet states and one singlet state, but the result is not 1/4. An intuitive explanation for why this is the case can be made by considering a single electron spin precessing in some random, constant magnetic field. Even though there are infinitely many different trajectories, all of them go through the original orientation. So the spin is more likely to be in its original orientation if we average over time compared to random

distribution of the spin direction. This geometrical argument explains experiments on muon spin relaxation. If we assume an ensemble of spin-1/2 particles polarized in one direction , and each is coupled to a bath of interactions approximated as random static magnetic fields from a 3D Gaussian distribution, then the decay of the polarization can be calculated exactly and it approaches 1/3 in the long time limit. This result is known as the Kubo-Toyabe function[12,13]. Similarly, for two spins, they are more likely to be in the singlet state that they started in. If they each couple to random fields from a 3D Gaussian distribution, then the singlet ratio approaches 1/3 in the long time limit[14].

Thus an external field that is much larger than the hyperfine fields increase the long time singlet ratio by 50%. However, the magnitude of MFE observed experimentally is determined by many other factors such as singlet decay rate and diffusion coefficient. Usually the decay rate is on a similar time scale as the rate of ISC, so the MFE is sensitive also to the rate of ISC and not just the long time limit singlet ratio.

One may ask whether static magnetic field can enhance ISC rather than suppressing it. It was proposed by our lab that high magnetic field gradient can achieve this goal. The idea is that large change of magnetic field over a short distance makes the electrons of the radical pair experience different local fields. The gradient then acts effectively like the hyperfine field and induce ISC. High field gradients can be found near magnetic nanoparticles or at boundaries of magnetic domains. The details of the theory can be found in ref. [14].

At high field, static magnetic field can also enhance ISC if the electrons have different g-factors, because they then precess at different rates. This is referred to as the Δg mechanism. The hyperfine and Δg mechanism can occur in the same system. In which

case one would observe increase in fluorescence with increasing field at low field. Then the hyperfine mechanism saturates and fluorescence is constant with increasing field strength. As the field increases further, Δg mechanism become important and fluorescence decreases[4,5].

In certain systems, the singlet and triplet states may not be completely degenerate if there is residual exchange interaction. External field can bring T_- to become degenerate with the singlet state. Therefore ISC is initially increased with increasing field until the Zeeman splitting matches exchange splitting. Then ISC decreases as the field splits T_- further away from S_0. This is referred to as the level crossing mechanism[2].

The hyperfine mechanism predicts increasing fluorescence intensity with increasing field. However, for certain systems, for very low field strength, the fluorescence initially drops with increasing field due to higher rate of ISC. This is known as low field effect (LFE) [15,16]. It can be understood intuitively by considering a single electron spin precessing about its local hyperfine field. It traces out a circle on the Bloch sphere. The application of a weak field sets the nuclear spins in a slow precession about the external field. So the electron spin, as it continues to precess about the hyperfine field due to the nuclear spins, traces out a greater area on the Bloch sphere. The effect of this on the electron pair is that they deviate more from the initial singlet state, and ISC is enhanced. This effect generally requires longer time between electron transfer and recombination, because nuclear spins precess much more slowly compared to electron spin.

This section has presented the basics of the radical pair mechanism. There are many extensions and variants of the basic mechanism for explaining experimental results

in many different systems. We refer to the many references that explain those theories in detail[2,3,17,18]. In the next section, we discuss the experimental observations using various techniques.

1.3 Observations of magnetic field effects (MFE) and related phenomena

There are many acronyms in describing magnetic effects in chemistry. They have been identified as they initially appear in the text. We collect these acronyms in table 1.1 for reference. The possibility of magnetic effects in biology has attracted much attention and effort. We briefly review the ideas and studies in that field in section 1.4.

Table 1.1 List of acronyms related to magnetic field effects

Acronym	Stands for
MFE	Magnetic field effect
ISC	Intersystem crossing
LFE	Low field effect
MIE	Magnetic isotope effect
CIDNP	Chemically induced dynamic nuclear polarization
CIDEP	Chemically induced dynamic electron polarization
ODMR	Optically detected magnetic resonance
RYDMR	Reaction yield detected magnetic resonance
ODESR	Optically detected electron spin resonance

1.3.1 Magnetic field modulated fluorescence

Systems that give off fluorescence are commonly studied because it provides a simple detection method. Our experiments also focus on fluorescent systems. The measurements will be presented in section 2. Here we briefly review some relevant experimental studies in the literature. Relatively few chemical systems display magnetic field effects because they need to be in the right range of parameter space, which include parameters such as radiative and non-radiative decay rates, diffusion coefficient, hyperfine field strength, and exchange integral. Molecules that are commonly used as electron acceptors include pyrene[19] and anthracene[20]. Typical electron donors include dimethylaniline (DMA) and indole molecules[21]. At relatively low field, hyperfine mechanism is the dominant mechanism, therefore external field increases fluorescence intensity. Measuring fluorescence intensity as a function of field strength yields information about the hyperfine fields of the system. There are some other important considerations which are also interesting research directions.

MFE requires a delicate balance of time scale, especially that of diffusion and ISC. Diffusion coefficient can be affected by viscosity and dielectric constant of the solvents or external factors such as temperature. The dielectric constant matters because the radical pair is charged, and the two radicals experience Coulomb attraction. High dielectric constant effectively shields the attractive force so the pair is more likely to diffuse apart. Low dielectric constant solvent leads to a stronger Coulomb force so the pair is more likely to stay close together. The requirement for MFE is that the pair first needs to diffuse away sufficiently far so exchange integral becomes small, and then they need to come back together to recombine. Therefore, it is not surprising that measurements of magnitude of MFE as a function of dielectric constant shows a peak at some optimal dielectric

constant[22,23]. Usually the dielectric constant is scanned through a range by mixing two solvents in different proportions. The timescale of ISC can also be tuned by substituting in isotopes to change the hyperfine fields. A common strategy is to substitute hydrogen with deuterium to reduce hyperfine field[24].

In the description above and in section 1.2, we described the case in which the reencountering radical pair is the original pair that experienced electron transfer. Thus their spin states are correlated and subject to the effect of magnetic field. This process is referred to as geminate recombination. The recombination could also happen between a pair that had different electron transfer partners. In that case, the spins states are not initially correlated and magnetic field has no effect. This is referred to as homogenous recombination. Since fluorescence from homogeneous recombination is not sensitive to magnetic field, it contributes to the background. There are different ways of reducing homogeneous recombination. One is to covalently link the donor and acceptor and ensure geminate recombination. We have also synthesized new molecules for this purpose. The synthesis and measurement results are presented in chapter 4 and 5, respectively. Different chained systems have been synthesized to study the effects of chain length, temperature, solvent, and high magnetic field[25-29]. An alternative that does not require chemical synthesis is to use micelles. In each micelle the number of donors and acceptors is small, and the ratio of geminate recombination is increased. Micelles also provide different environments compared to homogenous solvents[30-32].

In section 1.2 we distinguished between direct exciplex fluorescence and delayed fluorescence. The studies mentioned above are focused on direct fluorescence. Delayed fluorescence can also be measured with pulsed excitation source and time-resolved detection.

Since delayed fluorescence is from the triplet species, magnetic field decreases the intensity of delayed fluorescence[19,33]. The relative effect also tends to be larger because delayed fluorescence is proportional to the concentration squared. There are many other studies of magnetic field modulated fluorescence, for which we refer the reader to the references and the review papers.

1.3.2 Magnetic isotope effect (MIE), chemically induced dynamic nuclear polarization (CIDNP) and chemically induced dynamic electron polarization (CIDEP)

Different isotopes have different nuclear magnetic moments and produce different hyperfine fields. Therefore the ratio of singlet to triplet states can be altered by the presence of different isotopes. This is a new mechanism for nuclear isotope effects, because it is the nuclear magnetic moment rather than the mass difference that matters. We describe an experiment in 1976 by Buchachenko et al. to illustrate MIE[34]. Dibenzyl ketone (DBK) in solution mixture of benzene and hexane undergoes photodecomposition reaction. The excited DBK dissociates and initially form a triplet radical pair. The system can go through ISC and be in the singlet state, and then recombine into the starting molecule of DBK. If ISC does not happen, then the radical pair dissociates and decays via other pathways that do not lead to the formation of DBK. ^{12}C does not have a magnetic moment and does not contribute to the hyperfine field. ^{13}C is magnetically active, so its magnetic moment enhances ISC and leads to more DBK formation. Therefore we expect the DBK molecules that survive the decomposition process are more likely to have begun with the ^{13}C isotope. It was observed that ^{13}C concentration in DBK increases as the reaction proceeds, with enrichment of up to

17.6%. The application of an external field suppresses ISC and decreases the enrichment as expected. Later experiments also show that MIE of decomposition of DBK can be greatly enhanced when the radical pair is generated in micelles[35].

CIDNP refers to the phenomena that the NMR spectra of certain reacting systems show enhanced emission and absorption, due to non-Boltzmann distribution of nuclear spins. The phenomenon was originally observed by Bargon et al.[36] and Ward and Lawler[37]. The RPM can provide a basic explanation of CIDNP in similar fashion to MIE. Consider radical pair with nuclear states denoted by N_1 and N_2, which differ by spin 1 on one of the nuclei. The NMR signal from that nucleus would show enhanced emission or absorption if the ratio of N1 to N_2 does not follow the Boltzmann distribution in the products of the radical pair. Since the nuclear spin states determine the probability of products formation, different products from the reaction pathways of the radical pair have different ratios of N_1 to N_2 that are non-Boltzmann, leading to CIDNP signals. A key application of this phenomenon is photo-CIDNP applied to proteins. The experiment involves adding flavin dyes to proteins in solution. Upon photoexciation, the flavin dyes can form radical pairs with certain amino acid side chains, such as tyrosine, histidine, and tryptophan. The CIDNP effect enhances the NMR lines belonging to these amino acids. This process only happens when these residues are at the surface and exposed to solution. Therefore this technique provides a way to distinguish bwteen residues at the surface and residues buries inside the protein, thus the surface structure of the proteins can be probed [38,39].

CIDEP is the analogous phenomena for electrons. It can also arise from the RPM, but the underlying mechanism is different from CIDNP. Consider the density matrix of radical pair expressed in the basis of singlet and triplet states. With sufficiently high external field B

the $T_{\pm 1}$ states are split away and only the S and T_0 states are relevant. We shall consider the system that starts with fixed population in the S and T_0 states, and no off-diagonal coherences. The spin states then evolve first with the radical pair well separated and exchange interaction is negligible, then as the radical get close to each other, the spin Hamiltonian is dominated by the exchange interaction. In this situation the total polarization of the two electrons is not changed with the spin evolution, and CIDEP signal is only observed if the electrons have different g values [40]. The observable is the polarization of the two individual electrons, given by:

$$P = \rho_{ST}(t) + \rho_{TS}(t) . \tag{1.3}$$

Now first consider the spin Hamiltonian when the radical pair is far:

$$H_Q = B(g_1 S_{1z} + g_2 S_{2z}) + \sum_{i=1}^{N_1} A_i I_i \cdot \mathrm{S}_1 + \sum_{k=1}^{N_{21}} A_k I_k \cdot \mathrm{S}_2 . \tag{1.4}$$

This is just the combination of the Zeeman and hyperfine terms. It maps the population $\rho_{SS}(t) - \rho_{TT}(t)$ onto the coherence $\rho_{ST}(t) - \rho_{ST}(t)$. The Hamiltonian when the radical pair is close together is dominated by the exchange interaction:

$$H_J = J(\mathrm{S}_1 \cdot \mathrm{S}_2) \ . \tag{1.5}$$

It rephases the coherence, so the actions of the two Hamiltonians can be summarized as:

$$\rho_{SS}(t) - \rho_{TT}(t) \underset{\Leftrightarrow}{Q} \rho_{ST}(t) - \rho_{ST}(t) \underset{\Leftrightarrow}{J} \rho_{ST}(t) + \rho_{ST}(t) . \tag{1.6}$$

We can see that the combined effect of applying the two Hamiltonians in sequence is to map the original population difference onto the observable which is the individual electron

spin polarization[40]. We refer to these references[41,42] for more details of the theory and experimental observations of CIDNP and CIDEP.

1.3.3 Optically detected magnetic resonance (ODMR) and reaction-yield detected magnetic resonance (RYDMR)

Besides static field, one may also ask whether weak oscillating fields can affect chemical reactions. This is particularly relevant considering that we are exposed to electromagnetic radiation from electronic devices on a daily basis. Consider the energy level diagram in Fig.

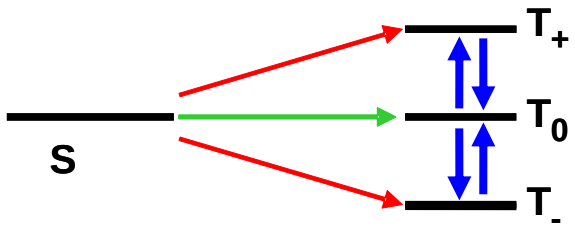

Fig. 1.4 Intersystem crossing in presence of external DC magnetic field and on-resonance oscillating field in an orthogonal direction

2b). The $T_{\pm1}$ states are split away and inaccessible when the splitting is large compared to the local effective magnetic field. But oscillating field on resonance with the splitting drive transitions to the $T_{\pm1}$ states and ISC can be enhanced, as shown in fig. 1.4, where the blue arrows illustrate the effect of the oscillating field.

In a fluorescent reaction with static external field, the application of resonant oscillating field would enhance ISC, and decrease fluorescence. If the oscillating field is continuously applied, and the DC field is swept, then a fluorescence drop would be observed as the DC field goes through the resonance. This is the phenomenon of optically detected magnetic resonance (ODMR), or also referred to as optically detected ESR (ODESR)[43,44]. Though

optical detection provides the best sensitivity, the reaction does not need to be fluorescent, in which case the reaction yield can be monitored to reveal the electron spin resonance[45]. This class of phenomena is referred to as reaction yield detect magnetic resonance (RYDMR).

In order to observe RYDMR, the magnitude of the oscillating field B_1 needs to be sufficiently large to rotate the electron spins within the lifetime of the radical pair. For a lifetime of 100 ns, this translates into a B_1 of the order of 10 G. As B_1 further increases to the order of 100 G, ISC is suppressed by the oscillating field due to spin locking effects [46].

1.3.4 Spin catalysis

In normal magnetic field effects, the inhomogenous hyperfine fields induce ISC. Hyperfine fields are generally not very strong, on the order of 10 G. If other forms of inhomogenous interaction can be applied, then ISC can be enhanced or suppressed. One possibility is using high magnetic field gradients such that the members of the radical pair experience sufficiently different fields even with nanometer separation[14].

The interaction does not need to be magnetic, but just needs to have the form of: $H = a\,\mathbf{S} \cdot \mathbf{F}$, where $\mathbf{F}$ is a vector quantity that couples to the electron spins. The exchange interaction is exactly of this form. However, as discussed in section 1.2, the exchange interaction between two electron spins suppress intersystem crossing because the singlet and triplet states are the eigenstates of that interaction. For just two spin interacting, the effective fields each spin experience is due to the other spin, and cannot induce ISC. But if there is a third spin in the vicinity of the radical pair, its exchange interaction with the two spins could be very different as H_J is very sensitive to distance. Therefore, a three spin system can exhibit

spin catalysis phenomena, where one spin acts as a catalyst for the other electron pair through the exchange interaction[47]. A first experimental demonstration was made when it was observed that the presence of TEMPO, a stable nitroxide radical, increased the probability of recombination of a radical pair that starts in the triplet state [48]. A related phenomenon is the inter-conversion between para- and ortho-hydrogen catalyzed by paramagnetic ions[49,50].

1.4 Magnetic field effects in biology

An important motivation for the study of magnetic effects in chemistry is to address the question whether ordinary magnetic fields influence biochemistry, and human physiology in particular. One area that has received much attention is magnetoreception for navigation in animals. It is known that many species, birds in particular, can sense the Earth's magnetic field for navigation purposes[51].

There are several hypotheses for the underlying mechanism, including detection by electromagnetic induction and biogenic magnetite based force sensing[52,53]. Chemical magnetorepection based on the RPM is of particular interest to us. The basic idea is that birds maintains magnetically sensitive chemical reactions, and infer direction with respect to the Earth's field by monitoring the reaction product[54]. Significant difficulties for this mechanism include the low strength of the Earth's magnetic field of about 0.5 G, and the fact that the MFE based on RPM is only sensitive to the magnitude and not the direction of the external field. The latter implies that at least one radical has to be immobilized, so that the system has an anisotropic response to the external field[55]. It has been demonstrated in vitro

under low temperature conditions that chemical systems can respond to magnetic field of the order of 0.5 G[56]. But no such system has been identified that functions under ambient conditions.

There are also many experimental evidences that favor a chemical magnetoreceptor over the competing hypotheses. Experiments show that the avian compass is dependent on the presence of light and its wavelength [57,58], and it is sensitive to the inclination with respect to the field lines, but not the polarity[59]. In other word, the avian compass would be insensitive to a flipping between the north and south magnetic pole, but could detect the angle with respect to the north-south axis. Furthermore, oscillating magnetic fields, which can affect chemical reaction through the mechanism of RYDMR, have been shown to interfere with the function of magnetoreception in birds[60].

These observations from behavioral studies are consistent with photo-initiated, oriented chemical systems based on the RPM, and are difficult to reconcile with the other theories. The main difficulty in further establishing the RPM hypothesis is to identify the biochemical process that is responsible for magnetoreception, which has remained elusive. One leading candidate is the protein cryptochrome which is found in the retina of migratory birds, and form photoexcited radical pairs[61-63]. However, there are also recent studies on neuronal response that offers evidence in favor of biogenic magnetite mechanism, and against the RPM hypothesis[64].

An important area where magnetic field effect due to the RPM is observed is in photosynthetic systems. It was shown that the hyperfine mechanism is responsible for magnetic field dependent decay of excited states in the photochemical reaction centers of *Rhodopseudomonas sphaeroide* [65,66]. Another example of magnetic influence on

biochemistry is the demonstration of MIE on ATP synthesis in vitro. The study compared the Phosphoglycerate kinase-directed ADP phosphorylation rates with the presence of $^{25}Mg^{2+}$ and $^{24}Mg^{2+}$ ions, and found that ATP production is 2.6 times higher with $^{25}Mg^{2+}$[67].

There are many reports in the literature on evidence for biological effects due to weak magnetic field. The significant interest in this field is motivated by the question whether the electromagnetic fields that we are exposed to on a daily basis affect our health. However, there are relatively few attempts to independently replicate the experiments reported, and often such effort found that the original results are not reproducible [68]. Furthermore, the studies on biological effects cannot resolve the question without also identifying plausible mechanisms and the associated bio-molecules. This has been the important issue in this field and has attracted much effort over the past decade. The experiments in refs [56] and [67] do identify the underlying mechanisms, but they were carried out in non-physiological conditions, and the effects are unlikely to persist *in vivo*.

The RPM hypothesis for avian compass is currently a leading candidate for potential manifestation of MFE in biology, as it has gathered significant evidence in its favor [69]. But the identification of the bio-molecules and processes involved are stilled required in order to prove the theory.

Ch 2. Magnetic field effects on fluorescence

2.1 The pyrene / DMA system

One electron transfer system that we have worked with extensively is the pyrene / dimethylaniline (DMA) system. The chemical diagrams of the molecules are shown in Fig. 2.1. Pyrene and DMA function as electron acceptor and donor, respectively.

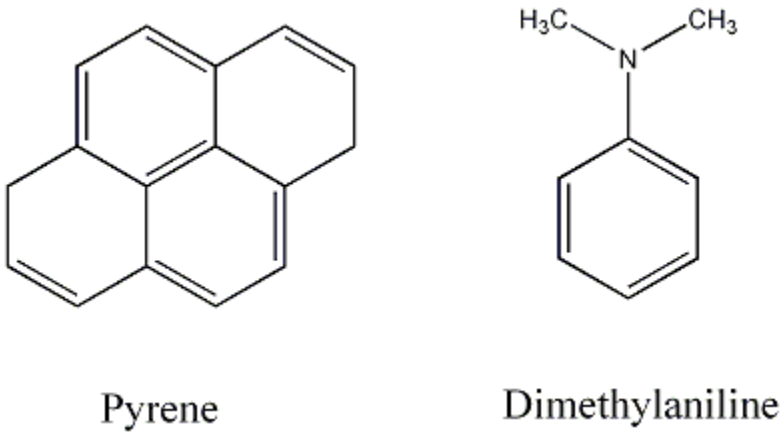

Fig. 2.1 Molecular diagrams of pyrene and DMA

Pyrene is the principle absorber of UV light. Its absorption spectrum is shown in Fig. 2.2. The absorption peaks are located at 241, 273, and 335 nm. We excite the molecule at around 335 nm, where the molar extinction is approximately 54000 cm^{-1}/M[70]. Pyrene is fluorescent and its excited state lifetime is on the order of hundreds of nanoseconds [71]. If the excited pyrene molecule encounters a DMA molecule before it has relaxed, then an electron transfer can take place from the DMA to the pyrene molecule, creating a radical pair that is initially in the singlet state. The radical pair can form a fluorescent exciplex if the spins remain in the singlet state. The exciplex fluorescence is broad, structureless, and red-shifted with respect to the prompt

fluorescence of pyrene. Therefore it can be spectrally distinguished from the prompt fluorescence directly coming from pyrene molecules in the excited state. Monitoring the exciplex fluorescence allows optical detection of MFE based on the radical pair mechanism (RPM) that was described in section 1.2.

Fig. 2.3 shows the fluorescence emission spectrum of pyrene at a fixed

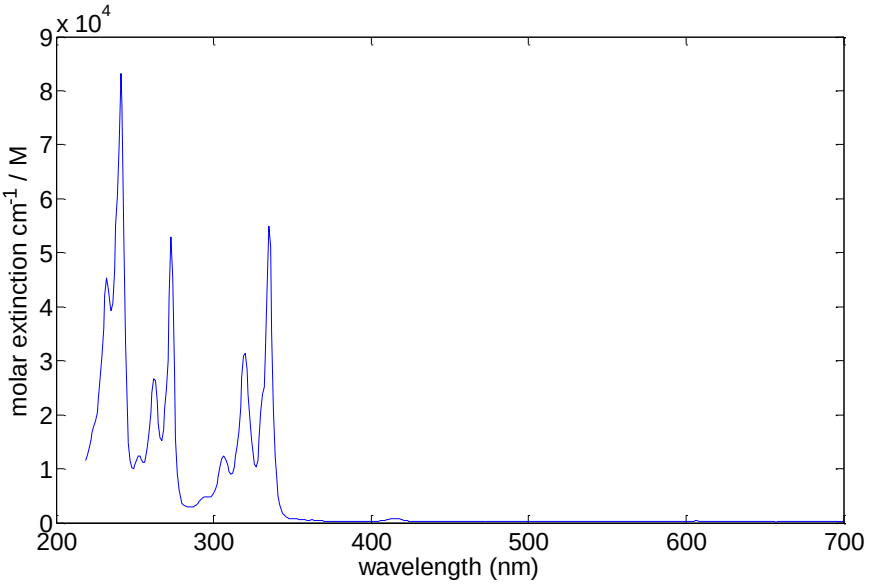

Fig. 2.2 Absorption spectrum of pyrene in cyclohexane.

concentration, and DMF at varying concentrations. The blue curve is the emission spectrum of pyrene as a standalone fluorophore. As the concentration of DMA increases, the fluorescence of pyrene is quenched, and the intensity of the broad exciplex fluorescence increases.

There have been many studies on MFE of the pyrene / DMA and related electron transfer systems[22,23,30,72]. The theoretical description of the MFE observed in the system based on the hyperfine mechanism has been worked out in detail[73,74]. The hyperfine fields on the pyrene molecule come from the 12 spin-½ protons, with hyperfine constants in the range of 2-5 G each. The ^{14}N contribute significantly to the hyperfine

field of the DMA, as it has spin 1, and hyperfine constant of approximately 12 G. The 11 protons on DMA have hyperfine constants in the range of 6-12 G each[74]. Fig. 2.4 adapted from Ref. [74] shows an illustration of the hyperfine fields on the pyrene / DMA pair. Each proton nuclear magnetic moment is represented by a small arrow, which point in random directions. The nitrogen magnetic moment is represented by a longer arrow as it is a spin-1 nucleus and has relatively large hyperfine constant. The total hyperfine field on each molecule is the vector sum of all the individual moments, and they are approximately 10 G and 30 G on pyrene and DMA, respectively. In absence of external field, the electrons on each molecule precess about the total hyperfine field. The

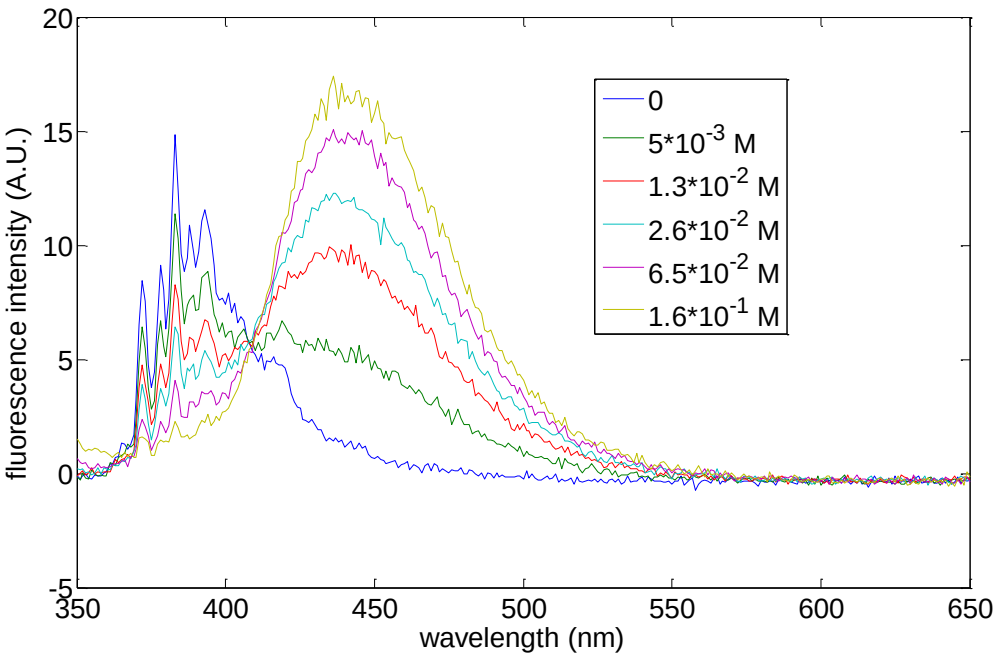

Fig. 2.3 Fluorescence intensity of pyrene at fixed concentration of 1×10^{-4} M, and varying concentration of DMA. Solvent is DMF.

difference between the hyperfine fields on pyrene and DMA then induces ISC.

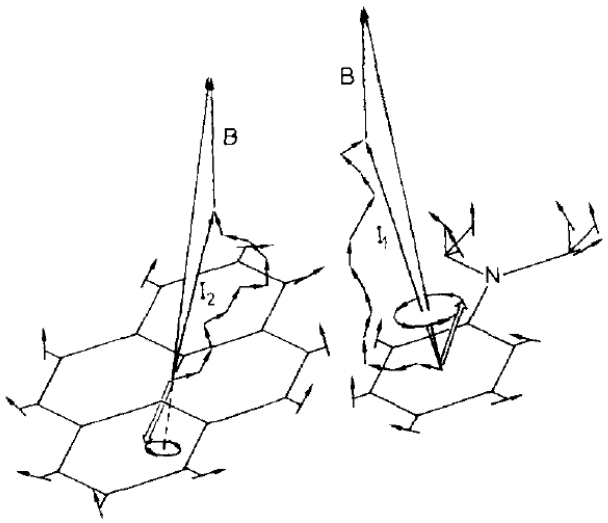

Fig. 2.4 Schematic illustration of the hyperfine fields on pyrene and DMA. From Ref. {{783 Schulten, K. 1978}}.

2.2 Steady state measurements

To measure MFE on fluorescence we need to monitor the exciplex fluorescence intensity as varying magnetic fields are applied. The magnetic field is applied by an electromagnet (GMW 5403) driven by a bipolar operational power supply with voltage programming (Kepco BOP 20-20 M). The sample is a solution of pyrene (1×10^{-4} M) and DMA (5×10^{-2} M) in a solvent mixture consisted of 75% THF and 25% DMF by volume. The sample is placed in a cuvette with septum screw-cap (Starna GL14-S). The sample is continuously degassed by bubbling with N_2 to purge oxygen, which quenches the radicals. The fluorescence is collected from the bottom of the cuvette by an optical fiber, and the light is directed through an emission filter (470 LP) onto an avalanche photodiode (APD, Perkin-Elmer SPCM-AQRH). The sample is excited by a 100 W mercury lamp with a 350 nm short pass filter (Asahi XUS0350). The mercury line at 334 nm coincides with the absorption peak of pyrene. All chemicals are obtained from Sigma-Aldrich with

the highest purity available and used without further purification. We use a data acquisition card (National instrument DAQ6259) to record the photon counts from the APD, and generate voltage signals to control the magnetic field. As the magnetic field is changed by the applied voltage, we record the actual field near the sample with a linear Hall-effect sensor (Alegro A1301).

The MFE measurement is shown in Fig. 2.5. The MFE on the y-axis is defined as the change in fluorescence normalized by the fluorescence when the applied field is zero. The curve observed can be explained by the hyperfine mechanism. The applied field lifts the degeneracy between the S_0 and $T_{\pm1}$ states. ISC is then inhibited and exciplex fluorescence is increased. The change in fluorescence is most rapid at relatively low fields when the external field competes against the hyperfine fields. As the applied field

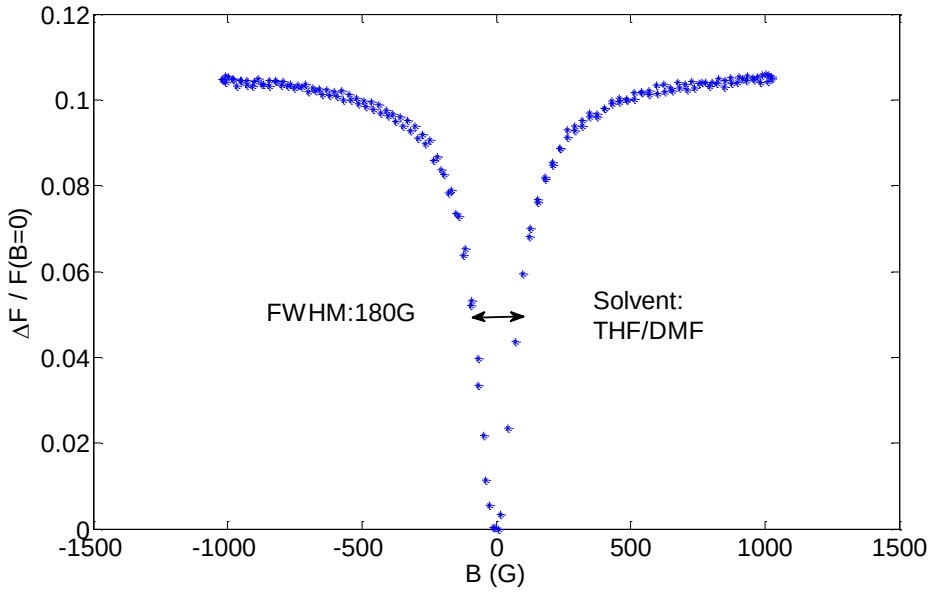

Fig. 2.5 MFE measurement of pyrene / DMA in a solvent mixture of 75% THF and 25% DMF

far exceeds the hyperfine fields, ISC to $T_{\pm 1}$ states is completely turned off, and further increase in applied field has no significant effect. The MFE is also sensitive only to the strength of the external field and not its polarity, as expected. The width of the MFE curve yields information on the strength of the hyperfine fields. We measure a FWHM of 180 G. This is larger than the value of 120 G obtained from theory and experiments in other solvents [19]. This could be due to solvent effects or different impurities in the sample.

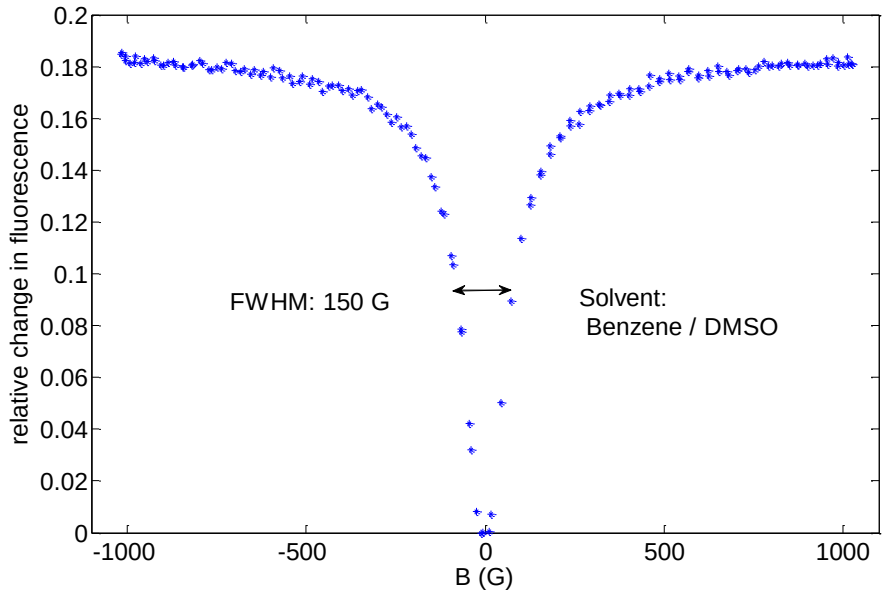

Fig. 2.6 MFE measurement of pyrene / DMA in a solvent mixture of 50% Benzene and 50% DMSO

As described in section 1.3.1, dielectric constant and viscosity of the solvent have a significant impact on the MFE curve. Since the radical pair is charged, dielectric constant ε has a particularly large effect on the diffusion process that is critical for MFE. In binary solvent mixtures, as the composition of the mixture is tuned, there is generally a particular composition that yields the optimal dielectric constant that maximizes MFE. At

lower ε, the Coulomb force is less shielded and it is difficult for the pair to diffuse sufficiently far apart for the exchange interaction to be negligible. If ε is too high, then the pair is less likely to reencounter after diffusing apart. The largest MFE for freely diffusing, intermolecular electron transfer system that we are aware of is pyrene / DMA in a solvent mixture of Benzene and DMSO as reported in Ref. [75]. The result measured with our setup is shown in Fig. 2.6.

The MFE in Benzene / DMSO can be as large as 18%. The FWHM of 150 G is also different from the value in THF / DMF. We have also experimented with other solvents. The alcohol solvents such as methanol and ethanol generally show much smaller MFE, on the order of 2-3%. Non-polar solvent such as cyclohexane do not have MFE. One promising mixture we identified that was not reported in the literature is 82% THF and 18% DMSO, which has a MFE of 12%, which is smaller than the benzene / DMSO mixture, but is less hazardous to use.

In general it is observed that solvent mixtures show larger MFE compared to solvents of a single component. It is suggested that the reason is the formation of micro-heterogeneous structures in solvent mixtures whose components have very different properties. Such structure has similar effects to micelles and suppresses homogeneous recombination which is insensitive to magnetic field[75].

If we use emission filters that pass the direct pyrene fluorescence at wavelength shorter than 400 nm, then no MFE is detected. This is because the fluorescence is from excited pyrene molecules that are not quenched by DMA. Therefore no radical pair is formed and its intensity is not affected by the magnetic field. However, in other systems, a MFE on the excited fluorophore is also observed. The magnitude is small compared to

the MFE on exciplex fluorescence. Since the external field only affects radical pairs, this demonstrates that there are interconversion between the excited fluorophore, exciplex, and radical pair [76].

2.3 Delayed fluorescence measurements

The measurements in section 2.2 are performed at steady state conditions. The sample is continuously excited and the DC fluorescence intensity is recorded. We refer to the result as MFE on prompt fluorescence to distinguish it from delayed fluorescence that originates from the triplet states. As described in section 1.2, if the radical pair is in the triplet state at reencountering, then an electron back transfer can still take place to create triplet species, in this case triplet pyrene molecules. The triplet molecules can then be quenched non-radiatively by oxygen or other radicals, or encounter another triplet molecule and undergo triplet-triplet annihilation according to: $^{3}Py + {}^{3}Py \Rightarrow {}^{1}Py + {}^{1}Py^{*}$, where the number 1 and 3 denote spin multiplicity and * represents an excited molecule. Essentially if the overall spin multiplicity of the two encountering triplet molecules is singlet, then they can become a singlet ground and a singlet excited molecule[33]. The energy of the triplet molecule is less than the singlet excited molecule because of the exchange interaction between the two valence electrons. Therefore the requirement for triplet-triplet annihilation is that the energy of the triplet is more than half of the singlet excited molecule. The resulting $^{1}Py^{*}$ can then decay radiatively, which is delayed fluorescence.

There are several key differences between delayed and prompt fluorescence.

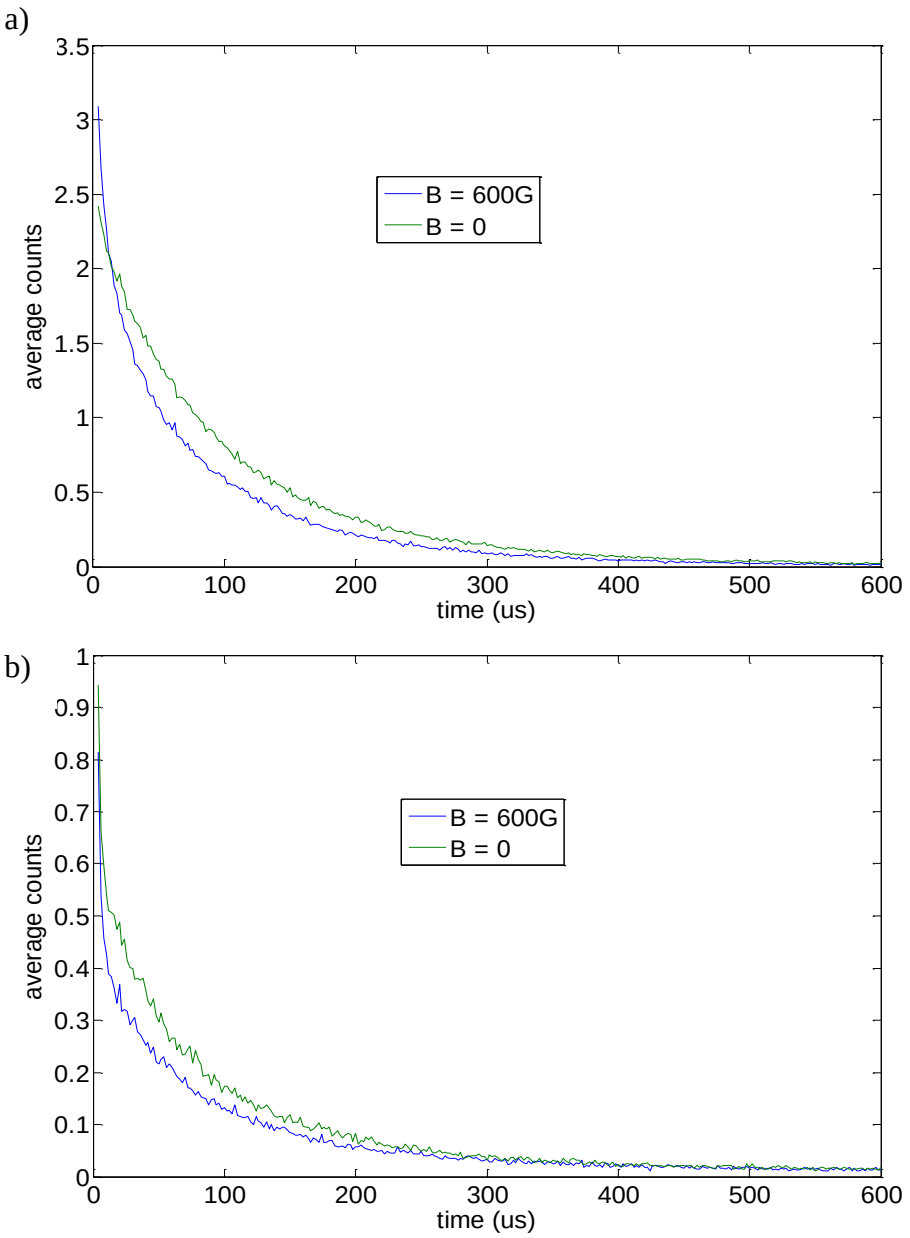

Fig. 2.7 a) MFE on delayed fluorescence of pyrene and DMA, in 82% THF and 18% DMSO b) MFE on delayed fluorescence of pyrene and DMA, in methanol

Since the source of delayed fluorescence is the triplet state, it is reduced by the external field. The triplet states are readily quenched by oxygen, therefore the observation of

delayed fluorescence depends on thoroughly purging the solution with inert gas. The magnitude of the MFE on delayed fluorescence is substantially larger than on prompt fluorescence, as the delayed fluorescence is proportional to the concentration of triplet species squared.

We adapt the setup as described in section 2.2. The excitation source is changed to a pulsed N_2 laser (VSL-337), with repetition rate of 20 Hz, pulse width of 4 ns, and pulse energy of 120 μJ. We gate the APD and count the photons in time bins of 2 μs. The measurements are shown in Fig 2.7. The solvent in a) is a mixture of THF / DMSO. We observe the reduction of fluorescence as expected. After the first 50 μs, the reduction is about 30%, which is much larger than the 12% MFE on prompt fluorescence. It is

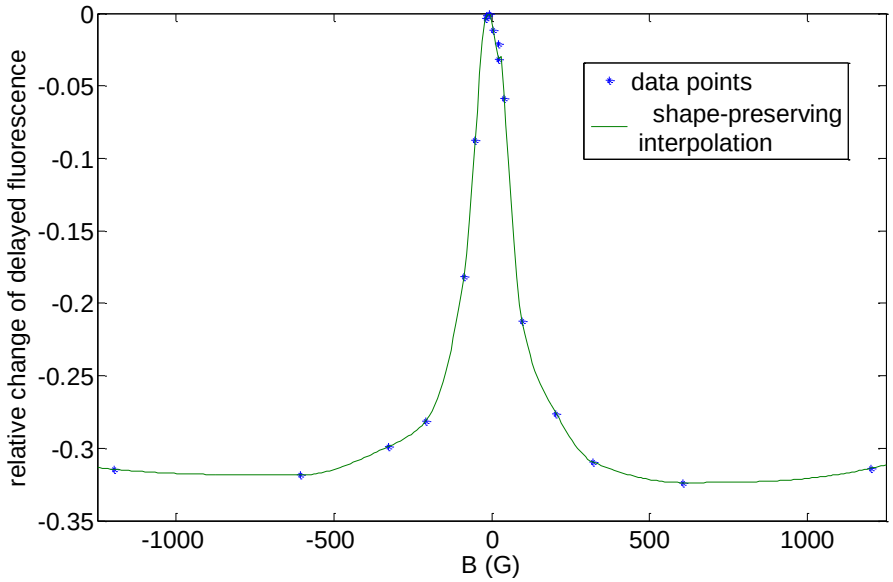

Fig. 2.8 MFE on delay fluorescence of pyrene and DMA as a function of applied field, the solvent is 82% THF and 18% DMSO

interesting to observe that for the first 10 μs the external magnetic field has enhanced delayed fluorescence. This is likely due to the tail end of the prompt exciplex

fluorescence, which is increased by the applied field and is much more intense than the delayed fluorescence under the experimental conditions. Fig. 2.7b) shows the result with solvent being methanol. There the fluorescence is reduced throughout the time observed as the lifetime of the exciplex is tuned by using different solvents.

In Fig. 2.8 we show the MFE on delayed fluorescence as a function of applied field. The relative change on the y-axis is defined as change in integrated delayed fluorescence after 50 μs normalized by the integrated delayed fluorescence after 50 μs when applied field is zero. The blue dots are the data, and the green interpolation curve is added as a visual aid. The curve has the features of what would be expected of the hyperfine mechanism except that the fluorescence is reduced. For freely diffusing systems, the relative MFE on delayed fluorescence is in general larger than that of prompt fluorescence. We have also experimented with variants of this system, using anthracene or phenanthrene as the electron acceptor, and 4,4‘ - bis(dimethylamino) diphenylmethane (DMDPM) as the electron donor. Pyrene and DMA is preferred for its large MFE and robustness, and is the system we use for works described in the following chapters.

2.4 The BBOT / TPD system

a)

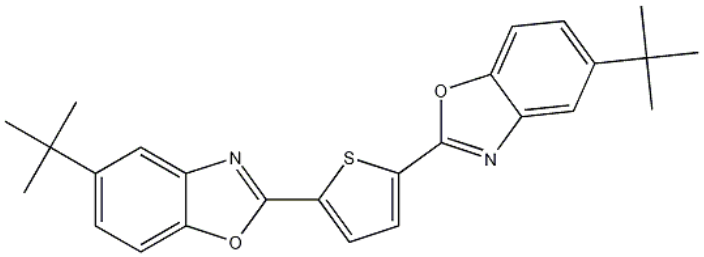

BBOT

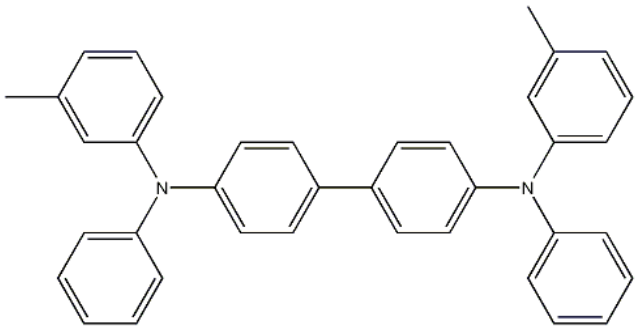

TPD

b)

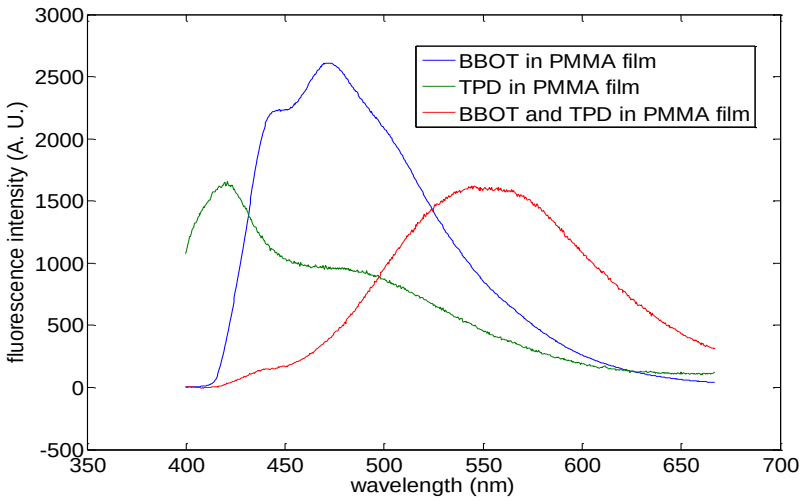

Fig. 2.9 a) Molecular diagrams of BBOT and TPD b) The fluorescence emission spectrum of BBOT only, TPD only, and the molecules in a 1:1 ratio, all samples are immobilized in a PMMA matrix, the red curve with both of the molecules show broad, structureless exciplex fluorescence centered near 550 nm

MFE on fluorescence provides a nice way of imaging the strength of the local magnetic field. The spatial resolution is set by the diffraction limit. One way to improve the spatial resolution is to use a chemical system that is in solid form and can be immobilized. Then if the fluorescence is collected from a thin layer of the chemicals, the spatial resolution in z is set by the layer thickness. Hu et. al. identified such an electron transfer system[77]. The molecules are 2,5- bis(5-tert-butyl-2-benzoxazolyl)-thiophene (BBOT) and N,N-diphenyl-N,N0-bis(3-methylphenyl)-[1,10-biphenyl] -4,40-diamine (TPD). Their molecular diagrams and exciplex formation are shown in Fig. 2.9. The MFE is observed when they are immobilized in a PMMA matrix at 1:1 ratio. We reproduced the result using our setup by replacing the cuvette with a glass slide with the sample on top. PMMA and the molecules are dissolved in chloroform and spin coated on the glass slide. We use 550/50 nm emission filter to capture the exciplex fluorescence.

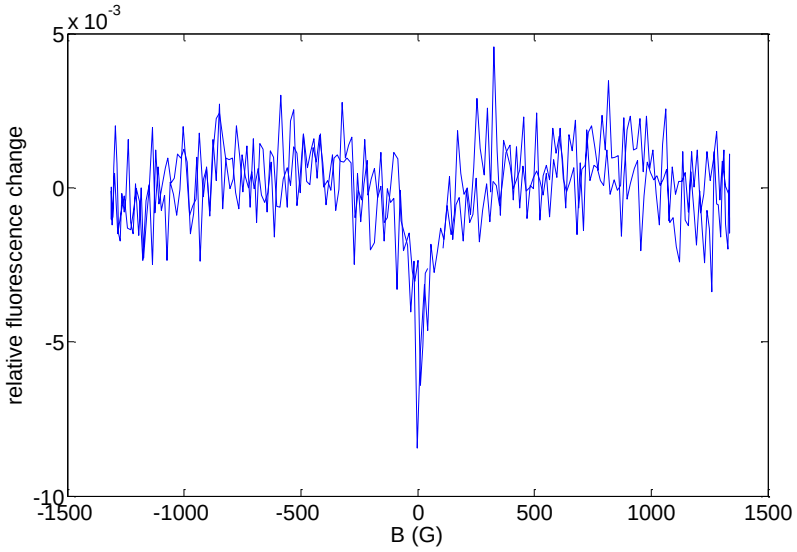

Fig. 2.10 MFE on fluorescence of the BBOT / TPD system. The molecules are immobilized in a PMMA matrix in 1:1 ratio

The MFE curve is shown in Fig. 2.10. The result is much noisier because of the low photon counts and the resulting large shot noise. It demonstrates that the MFE of the system is governed by the hyperfine mechanism. This is quite surprising for an immobilized system, since without diffusion, the exchange interaction remains significant and prevents intersystem crossing. In that case, observation of the level-crossing mechanism is also likely. One possibility is the transfer of excitation along the molecules, both of which have a chain structure linking similar parts together. Therefore it is possible for electron transfer to occur at one part of the molecule, and the excitation is transferred to another part slightly away from the other molecule, reducing the exchange interaction between the radical pair and allows the hyperfine mechanism to function.

Ch 3. Magnetofluorescence imaging (MFI)

3.1 Moltivation

Magnetic field modulated fluorescence allows an optical readout of the magnetic field strength. Unlike optical fields, static magnetic fields are not scattered by most materials. Based on this property, we proposed and demonstrated magnetofluorescence imaging (MFI), a method of imaging through scattering media via MFE on fluorescence. This chapter is based on Ref. [78]

We reasoned that an inhomogeneous magnetic field would lead to a spatially varying rate of ISC, and thereby to a spatially varying fluorescence. In particular, a field with a localized null leads to a localized region in which ISC is faster—and the fluorescence lower—than in its surroundings. We scan this field null through a sample chamber containing a non-magnetic object immersed in a magnetofluorescent fluid. We record the total fluorescence intensity as a function of the location of the field null. The pattern of fluorescence intensity indicates the shape of the object. Due to the small fractional changes in fluorescence expected during the measurement, we dither the location of the magnetic null at a high frequency and use lock-in detection of the fluorescence.

3.2 Experimental apparatus

Fig. 3.1a) shows a diagram of the apparatus. Four permanent dipole magnets (K&J Magnetics DX0X0-N52) produce an octupole field in which $\mathbf{B} = 0$ along the entire

z-axis. In the x-y plane, this arrangement creates a localized magnetic null at the origin. The magnets are cylinders with a diameter of 25.4 mm, a length of 25.4 mm, and a surface field of 6619 G. Opposing faces are 36 mm apart. Dithering coils are mounted

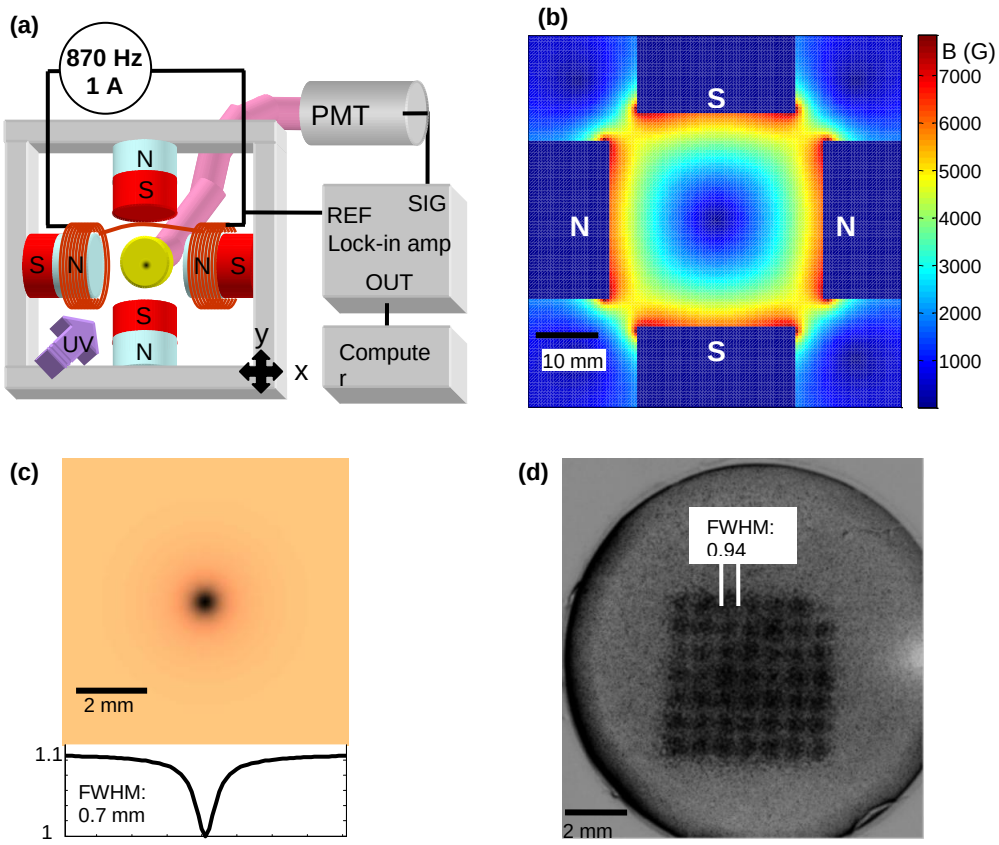

Fig. 3.1 Apparatus for magnetofluorescence imaging. a) The sample is immersed in a solution of pyrene/DMA (yellow disk) and placed in an octupole magnet. UV illumination impinges from above and fluorescence is sent via 10 mm acrylic light guide to a photomultiplier (PMT). Bias coils dither the location of the magnetic null at 870 Hz for lock-in detection. A mechanical x-y stage scans the magnet assembly relative to the sample. b) Simulation of the magnetic field strength due to the permanent magnets in the plane $z = 0$. c) Predicted point spread function based on field profile from (b), and the MFE on fluorescence from Fig. 1b. d) Direct optical imaging of the point spread function. The light guide and PMT were replaced by a CCD camera. The sample chamber was filled with pyrene/DMA and the exciplex fluorescence was imaged onto the camera. The octupole magnets were scanned across a 7 x 7 grid. The dark spots correspond to the locations of the null in the magnetic field. The point spread function has a FWHM of 0.94 mm.

concentrically with two of the magnets. Each coil is wound from 61 m of 18 gauge magnet wire. The inner and outer diameters are 4 cm and 8 cm, respectively. The coils are connected in series with a 4 μF capacitor for resonant driving. The octupole magnet and dithering coils are mounted on a Ludl precision scanning stage. The sample chamber, excitation and detection pathways are mounted to the optical table and do not move during the experiment. The magnet assembly is scanned relative to the sample.

The sample chamber is constructed from a ½" diameter black anodized aluminum tube (Thorlabs SM05L05) with top and bottom surfaces composed of optical windows (Anchor Optics AX45637). A size 12 Kalrez o-ring (VWR 14212-020) is placed between the windows to seal the fluid in the chamber and to set the separation of the windows to be 2 mm. The object to be imaged is immersed in a solution of pyrene/DMA contained in a sample chamber, which is mounted between the magnets. Ground glass windows (Edmund Optics NT62-616) are placed within the aluminum tube, 2 cm above and below the sample chamber. These windows scatter light strongly, and thereby prevent conventional optical imaging of the sample.

A 100 W mercury lamp with a 350 nm short pass filter (Asahi XUS0350) illuminates the top of the sample with 12 mW of UV light. The mercury line at 334 nm coincides with the absorption peak of pyrene. An emission filter (Chroma D435/90x) below the sample blocks transmitted excitation light and passes exciplex fluorescence to a 10 mm diameter acrylic light guide (Anchor optics AX27644), which carries the fluorescence to a photomultiplier tube (Hamamatsu H10492-013).

To acquire an image, the x-y translation stage moves the magnet assembly relative to the sample in a raster pattern, causing the dark spot to move across the sample. To enhance the signal-to-noise ratio we use a lock-in detection scheme. A function generator connects to an audio amplifier, which drives the dithering coils at 870 Hz and 1 A, r.m.s., corresponding to an AC field amplitude of 80 G at the magnetic null (see Supplementary Movie 3). Drive currents are chosen so the amplitude of the dithering is approximately half the width of the dark spot. The total fluorescence intensity develops a component at the modulation frequency only when the dithering carries the dark spot across the boundary of an object. The signal from the PMT is fed into a lock-in amplifier (Princeton Applied Research 5210), and the signal driving the dithering magnets is used as a reference. We use a Labview program to control a data acquisition card (National instrument DAQ6259).

We typically perform two x-y scans, with the sample rotated 90º about the z axis between each. The two outputs of the lock-in, acquired from corresponding points in the sample, are combined to associate a vector with each point. This vector points along the surface-normal of the object in the x-y plane.

We simulated the field of the permanent magnets by numerical integration of Maxwell's Equations in Matlab (Fig. 3.1b). The field distribution was combined with the measured MFE for pyrene/DMA to yield an estimated point spread function (Fig. 3.1c). The result agrees well with the point spread function measured by acquiring a fluorescence image of the sample chamber containing only pyrene/DMA solution (Fig. 3.1d). The dark spots in Fig. 3.2d) indicate the locations of the null in the field as the magnets are moved relative to the sample.

The symmetry of the octupole arrangement ensures that the magnetic null exists along the entire *z*-axis. The point spread function broadens away from the plane $z = 0$, but this broadening is negligible over the 2mm vertical dimension of the sample chamber.

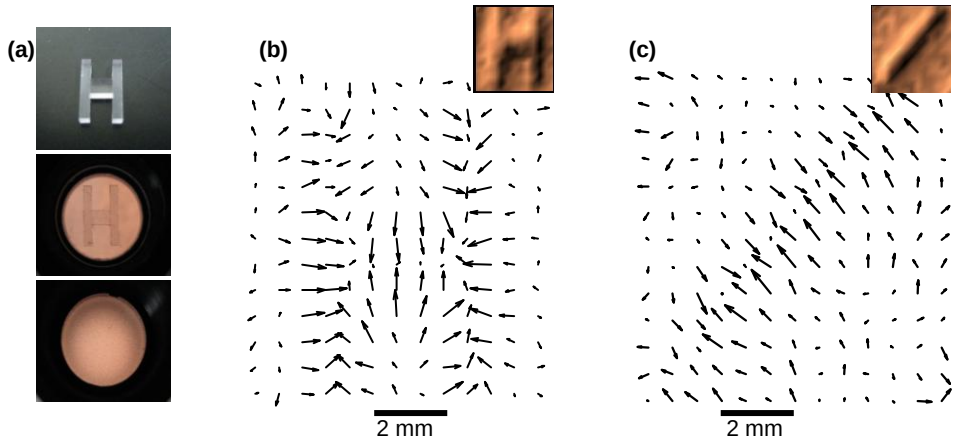

Fig. 3.2 Imaging through a scattering medium. a) Sample cell. A glass object to be imaged (top) is placed in a chamber with a solution of pyrene/DMA (middle). The bottom and top of the chamber are blocked by ground glass plates so the object is obscured (bottom). b) Magnetofluorescence images of the sample hidden inside the chamber. The vectors represent the local gradient of the MFE, which is only large at the solution / object interface. The quiver plot shows the boundaries of the object in (a). Inset: projected shadow image. c) Quiver plot showing the boundaries of a single glass rod. Inset: projected shadow image.

3.3 Result

MFI is insensitive to the path the light takes entering or exiting the sample, because the detection volume is determined entirely by the magnetic field. Thus one may acquire optical images in the presence of arbitrarily strong optical scattering. This property of MFI is dramatically demonstrated by imaging through our sample chamber,

in which the only optical access is through ground glass plates. MFI penetrates the walls of the chamber, yielding the images shown in Fig. 3.2.

The samples imaged in Fig. 3.2 are made by cutting a 1 mm thick glass slide into strips. A dilute solution of sodium silicate is used to bind the strips together. We first acquire an MFI image of the sample chamber containing only a solution of pyrene/DMA. Then we acquire an image with the glass sample. The difference between these images shows the boundaries of the sample. By projecting the surface-normal vectors onto a single axis (45° from vertical, in this case), shadow images of the object are created. We emphasize that these images could not have been acquired by conventional imaging due to the strong scattering of light entering and exiting the sample.

3.4 Discussion

The spatial resolution of MFI is given by $\delta x = \sigma / \nabla B_0$, where σ is the width of the MFE (in G) and ∇B_0 is the gradient in the field strength at the magnetic null (in G/mm). In our device, σ = 180 G and ∇B_0 = 260 G/mm, leading to a theoretical resolution of 0.7 mm. Our experimentally determined resolution is 0.9 mm. Steeper gradients or narrower magnetic response curves lead to higher resolution. A steeper gradient is obtained by either increasing the strength of the octupole magnets, or by decreasing their size and separation. Material limitations determine the maximum strength of the octupole permanent magnets, so miniaturizing the octupole magnets provides the best route to higher field gradients. Strong permanent magnets may be

fabricated down to the sub-micron scale, suggesting that the present system could be miniaturized by at least four orders of magnitude.

The number of resolvable spots along each axis is $N \approx \frac{L\nabla B_0}{2\sigma}$, where L is the distance between the pole pieces. The factor of 2 arises from the constraint that the sample must be no larger than $L/2$ along any dimension, to avoid collisions with the permanent magnets during scanning. Scaling the system to smaller size while keeping the magnetization fixed does not affect the number of resolvable spots because $L\nabla B_0$ remains constant. The present system generates images with 13 x 13 resolvable points. To increase the number of resolvable points one must increase the sensitivity of the MFE.

Molecules with smaller hyperfine fields respond to smaller magnetic fields, and thus enable higher resolution imaging. Deuterated molecules have significantly reduced hyperfine fields and have been demonstrated to show greater sensitivity to magnetic fields [16]. Other electron donor/acceptor systems show magnetic sensitivity to fields as small as 0.4 G [56]. An outstanding chemical challenge is to design fluorescent systems with greater magnetic field sensitivity. Ideally such systems would also be photostable and water soluble.

A further challenge in MFI is to detect the small fluctuations in the fluorescence at the magnetic null, above the larger unmodulated fluorescence from the remainder of the sample. In our experiment, the maximum AC component of the PMT voltage is V_{AC} = 100 μV, while the DC background is V_{DC} = 500 mV. To achieve a shot noise-limited SNR of 10, one must acquire at least $n_{phot} = 100(V_{DC}/V_{AC})^2$ fluorescence photons at each pixel. This requirement can lead to unreasonably long image acquisition times. The

background increases as $V_{DC} \propto N_{pix}$, where N_{pix} is the number of pixels, while the maximum AC signal is independent of N_{pix}. The acquisition time per pixel increases as N_{pix}^2, and the time per image increases as N_{pix}^3. Thus shot noise ultimately limits the number of pixels in an MFI image. To improve the signal-to-background ratio, one would like to increase the magnitude of the MFE. For our present system the MFE is about 10%. As we will describe in the following two chapters, covalently linking the donor and acceptor pair can dramatically increase MFE, to as much as 130%.

The signal-to-background ratio can also be improved by using a system in which the magnetic field *suppresses* fluorescence. For instance, the delayed fluorescence—in contrast to the prompt fluorescence used here—of pyrene/DMA is suppressed by a magnetic field [72]. Delayed fluorescence arises from radical pairs that undergo intersystem crossing into the triplet state. Electron back transfer leaves pyrene in an excited triplet state. When two triplet pyrenes collide, one pyrene can end up in an excited singlet state, which then emits delayed fluorescence. The timescale of delayed fluorescence is set by diffusional encounter of pairs of triplet pyrene, and is much longer than the prompt fluorescence lifetime of pyrene of ~100 ns. The intensity of delayed fluorescence is reduced by an external magnetic field.

The ability of MFI to image inside scattering media may prove useful in biomedical imaging, as biological tissues scatter light strongly. Optical coherence tomography, photoacoustic microscopy, optical phase conjugation, and wavefront shaping allow imaging through scattering media, but these techniques have depth of penetration of 1 mm or less [79-82]. MFI is in principle free from such limits, provided

molecules with suitable fluorescence spectra and magnetic sensitivities are identified. Furthermore, MFI only senses magnetically sensitive fluorophores, and is thus insensitive to crosstalk from other fluorescent compounds. The spatial resolution of MFI is entirely independent of the strength of the optical scattering, provided that a sufficient number of fluorescence photons reach the detector. One can also conceive of applying MFI in a semi-infinite medium, in which case fluorescence would be detected in the backscattered direction rather than in the forward direction.

Ch 4. Synthesis of linked donor-acceptor systems

4.1 Moltivation

The ideal system for studying magnetic field effects on fluorescence would have the following properties.

- Large MFE
- Same donor and acceptor partners with repeated excitations
- Absorption in the visible
- Bright and photostable
- Narrow MFE linewidth

Among these properties, brightness and photostability are generally intrinsic to the molecular systems. Significant improvements need to come from discoveries of new molecular systems that both have the right parameters to show MFE and better brightness and photostability. Narrow MFE linewidth means the system is more sensitive to the gradient of the magnetic field. This is helpful for imaging applications as well as oscillating MFE. The MFE linewidth is governed by the effective hyperfine field. Systems have been studied that are sensitive to the earth field and have low effective hyperfine field, but the experiment requires low temperature [56]. Since the hyperfine field is ubiquitous from hydrogen and C_{13} atoms, and is required for MFE, it is difficult to significantly reduce it.

On the other hand, improvements on the first three properties can be effectively achieved by the strategy of covalently linking the donor and acceptor by a molecular

chain. In a system where the donor and acceptor are not chained, once the radical pair is formed by electron transfer, the charged donor and acceptor can freely diffuse relative to each other. At reencountering, there are two possibilities. The donor / acceptor pair could be the original pair that experienced the electron transfer, in which case their starting spin state was singlet. If they have remained in the singlet at reencountering, an electron back transfer could occur and relax the system back to the ground state. This is referred to as geminate recombination, and is sensitive to external magnetic field as described before. The other possibility is that the reencountering pair has different partners that they have diffused from. In this case their spin states are not correlated. The radical pair has a 1/4 chance to be in the singlet state and is not sensitive to external magnetic field. Combination through this path is called homogeneous recombination. Therefore homogeneous recombination contributes a background that is insensitive to magnetic perturbation. In unchained systems, this background is significant. Covalently linking the donor and acceptor ensures that the vast majority of recombination is geminate, hence increase the MFE signal.

The fact that electron transfer is intramolecular rather than intermolecular also ensures that, with repeated excitations, the donor and acceptor partners remain the same. This is useful because the nuclear spin configuration of the pair is preserved. We proposed an experiment to take advantage of repeated rounds of excitation and ISC in a chained donor-acceptor system.

The rate of intersystem crossing is a function of nuclear spin configuration which determines the hyperfine field. If the hyperfine field experienced by both electrons is similar, ΔB_{hf} is small, then the electron spins precess in sync and intersystem crossing is

slow. If the hyperfine fields are very different, ΔB_{hf} is large, then ISC occurs quickly. The experiment involves repeatedly exciting the molecules and monitoring the nuclear spins states. The timescale of nuclear spin relaxation is typically on the order of 0.1-1 seconds, which is long compared to the electronic processes. So we can assume that the nuclear configurations is essentially the same during the experiment. We expect the pairs with small ΔB_{hf} to be more likely to remain in the singlet state, relax back to the singlet ground and can be excited again. The pairs with large ΔB_{hf} are more likely to go into the triplet state and do not come back to the singlet ground. Repeated excitation would preferentially reduce the population with large ΔB_{hf}, so the pairs that have remained in the singlet ground state would have a non-thermal distribution of nuclear states.

This procedure selects for pairs that have similar hyperfine fields on both the donor and acceptor. However, unlike the non-Boltzmann distribution resulting form nuclear hyperpolarization, no polarization takes place, which makes monitoring this non-thermal distribution difficult. This experiment would not work if the donor and acceptor are not linked. Then one acceptor has a different partner donor with each excitation. The relative nuclear configuration changes each time and the process would not select for anything. This proposed experiment illustrates why always having the same donor and acceptor pair is a useful property. One way of overcoming the difficulty of detecting the non-Boltzmann distribution without polarization is to exploit its effect on ISC and fluorescence. Since pairs with similar hyperfine fields are selected for, the rate of ISC in the remaining pairs is low compared to a thermal distribution of hyperfine fields. Therefore the magnitude of MFE should decrease as this nuclear spin selection process

continues. This should be carefully distinguished from potential artifacts such as sample degradation.

When attaching the donor and acceptor with a molecular chain, the acceptor is chemically modified, so we expect its absorption spectrum to shift. Typically the acceptors absorb in the UV, so if there is sufficient red shift we can expect systems with

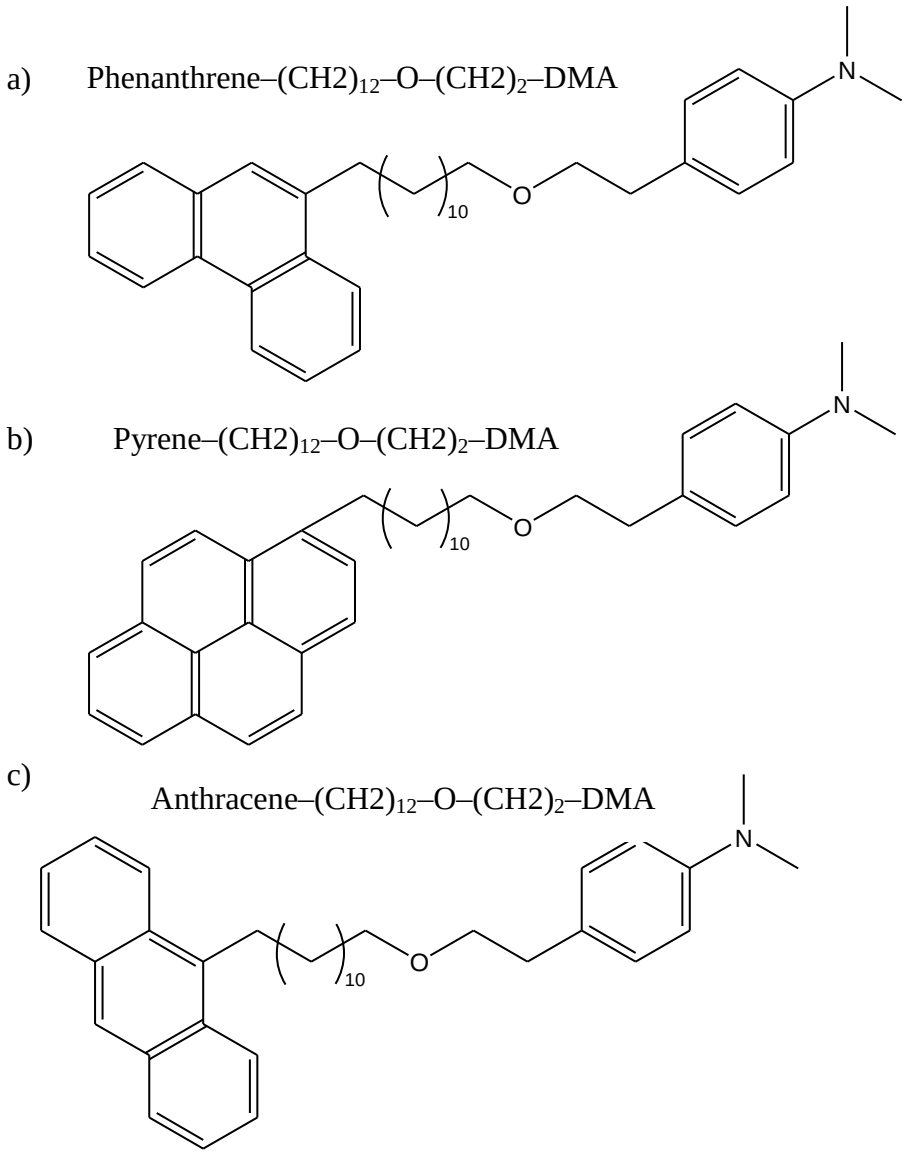

Fig. 4.1 Molecular structures of the three synthesized compounds.

visible absorption. Therefore, a compound that consists of a donor and an acceptor linked by a molecular chain offers many advantages over the freely diffusing systems.

Different chained systems have been synthesized to study the effects of chain length, temperature, solvent, oscillating field, and high magnetic field[25-29,46]. Such systems can display MFE as large as 140% compared to about 10% in unchained systems[28].

4.2 Synthesis procedure

We chose to adapt the synthesis procedure from Cao et. al. [28], because the molecule they studied, phenanthrene-$(CH_2)_{12}$-O-$(CH_2)_2$-DMA, displays the largest MFE on fluorescence. The molecules we synthesized are of the general form acceptor-$(CH_2)_{12}$-O-$(CH_2)_2$-DMA, where the acceptor is phenanthrene, pyrene, or anthracene. The molecular structures of the compounds are shown in Fig. 5.1.

The synthesis is completed in two parts as illustrated in Fig. 5.2. For the first part, 2.6 g of 9-bromophenanthrene was added to an anhydrous diethyl ether solution in a flask kept in an ice bath. 12 mL of 1.6 M hexane solution of n-butyllithium was added drop wise. The mixture was stirred for 4 hrs. 15 g of 1,12-dibromododecane was added as once. The mixture was stirred for several minutes, and the flask is placed in a water bath at 30°C and fitted with a reflux condenser. The solution is refluxed for 2 hrs. The reaction mixture is extracted by diethyl ether. The organic layer is washed by distill water for three times, then washed by brine solution, and dried over magnesium sulfate. The diethyl ether is evaporated. The crude reaction product is purified by column

chromatography on silica, with hexane as the solvent, yielding phenanthrene-12-Br as the product of the first part.

1 g of NaH (60% oil suspension) was dissolved in 20 mL of N,N-dimethylacetamide. 1 g of phen-12-Br and 0.5 g of 2-[4-(dimethylamino)phenyl]-ethanol were added to the solution and the mixture is stirred for 4 hrs in an ice bath. The reaction mixture is extracted by diethyl ether. The organic layer is washed by distill water for three times, then washed by brine solution, and dried over magnesium sulfate. The crude reaction product is purified by column chromatography on silica. The solvent used is a

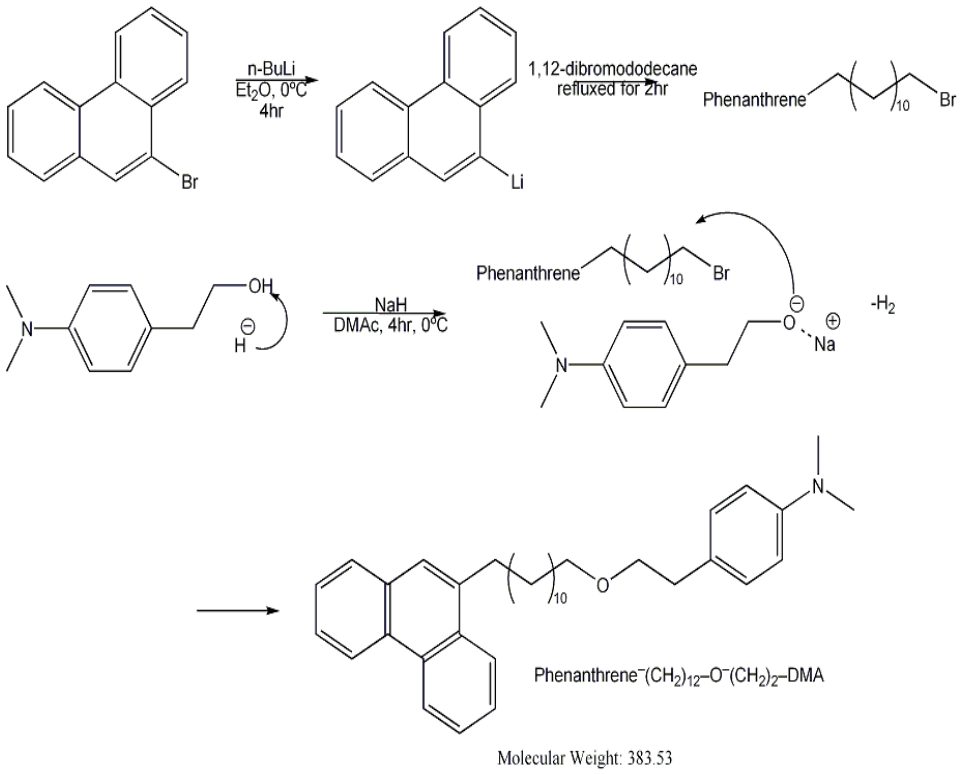

Fig. 4.2 Synthesis procedure of phenanthrene-$(CH_2)_{12}$-O-$(CH_2)_2$-DMA, drawing by Vijay Jain.

mixture of hexane and ether in 9:1 ratio. The purified product of phen-12-O-2-DMA is obtained as a white crystal.

Proton NMR ($CDCl_3$, 500 MHz) on the final product is shown in Fig. 5.3. The following peaks can be identified: δ=8.76-7.58 (9H on phenanthrene), 7.12-6.74 (4H on benzene ring), 3.59-3.42 (4H O-CH_2), 3.14-3.08 (2H phen- CH_2), 2.92 (6H CH_3), 2.84-2.72 (2H DMA- CH_2), 1.84-1.22 (20H protons on the chain). We have also performed

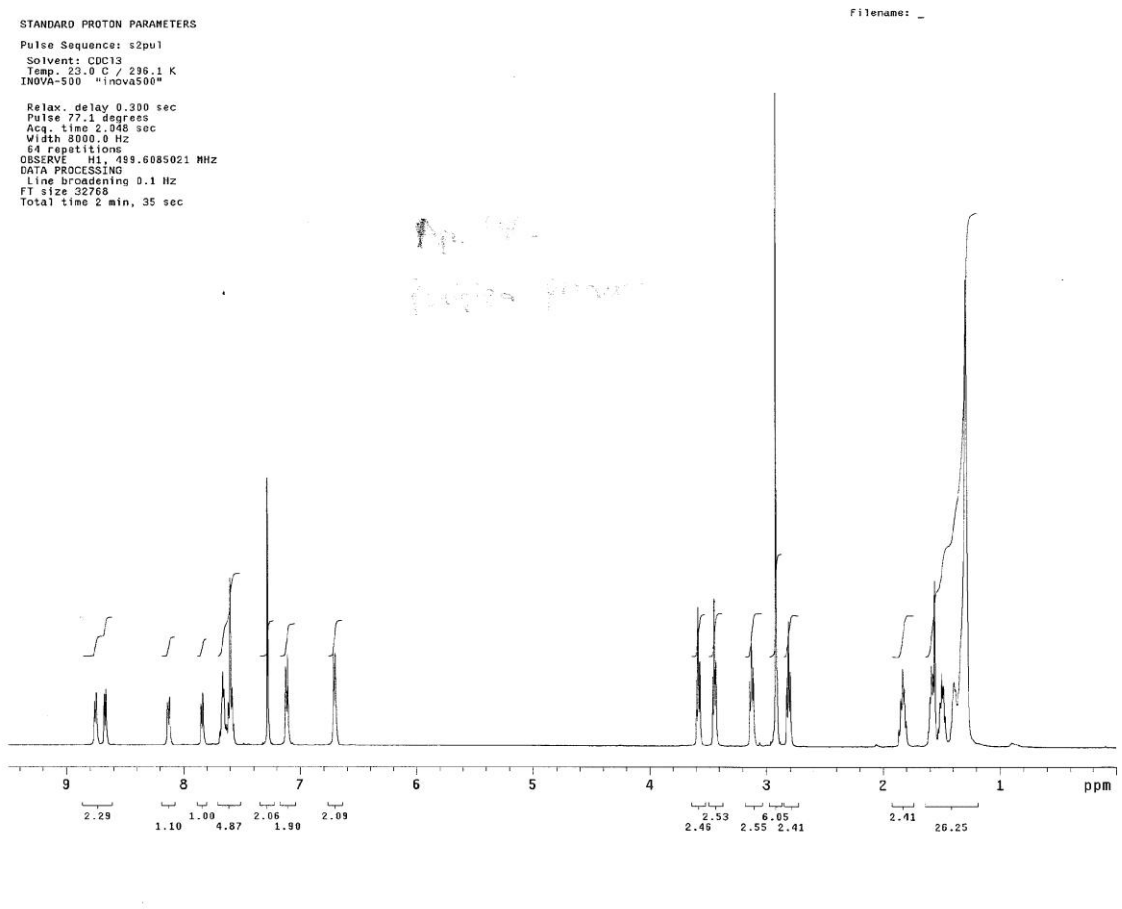

Fig. 4.3 Proton NMR ($CDCl_3$, 500 MHz) spectrum of the purified product of phen-12-O-2-DMA. The peak at 7.24 ppm is from impurities of undeuterated chloroform in the solvent.

mass spec analysis that confirms the elemental composition of the product with error of about 1 ppm.

Similar procedures are applied to synthesize pyrene and anthracene versions of the compounds. The starting materials for those compounds are 1-bromopyrene and 9-bromoanthracene, respectively. All chemicals for synthesis are from Sigma-Aldrich with the highest available purity, and used with no further purification.

Sometimes the second reaction failed to produce the desired products, and the component containing the acceptor would display broadened NMR peaks. This problem is particularly pronounced for anthracene. We found that neutralizing the NaH in the mixture with HCl until pH reaches 7 improves the success rate, and have incorporated this step into the synthesis protocol.

Ch 5. Characterization of linked donor-acceptor systems

We make various MFE measurements on the three different chained compounds mentioned in chapter 4. The electron donor in all three is N,N-dimethylaniline (DMA). The compounds are of the form acceptor-$(CH_2)_{12}$-O-$(CH_2)_2$-DMA, where the acceptor is phenanthrene, pyrene, or anthracene. In addition to measuring MFE on fluorescence in both steady state and time-resolved experiments, we also measured MFE on transient absorption due to the triplet states. We find that the magnitude of MFE on singlet fluorescence and triplet absorption are negatively correlated. This suggests that the difference in MFE among the three molecules can be explained by the different ratios of singlet to triplet generated. This also points to potential directions for engineering molecules that display particularly large MFE in either fluorescence or transient absorption.

5.1 Steady state MFE measurements

The steady state MFE curve as a function of magnetic field is measured with the setup described in section 2.2. For measurements with varying excitation or emission wavelengths, we use a Cary Eclipse spectrophotometer. The sample is held in a 1 cm square quartz cuvette. Excitation and emission collection are at the sides of the cuvette in directions orthogonal to each other. We apply magnetic field by placing a 1 cm square neodymium magnet at the bottom of the cuvette. The surface field of the magnetic is about 1000 G. The upper parts of the cuvette is blocked so emission collection only comes from the region within 1 cm of the surface of the magnet.

Among the three chained donor-acceptor systems, phenanthrene-12-O-2-DMA displays the largest MFE. In fig. 5.1, we compare its MFE signal with the unchained pyrene / DMA system. The excitation wavelength is 355 nm. As anticipated, MFE in the chained compound is significantly higher. There are two interesting features of the MFE curve of the chained compound. The FWHM is about 400 G, which is significantly higher than the unchained compound; and the fluorescence level continues to rise even at relatively high fields. Both of these features imply large effective hyperfine fields.

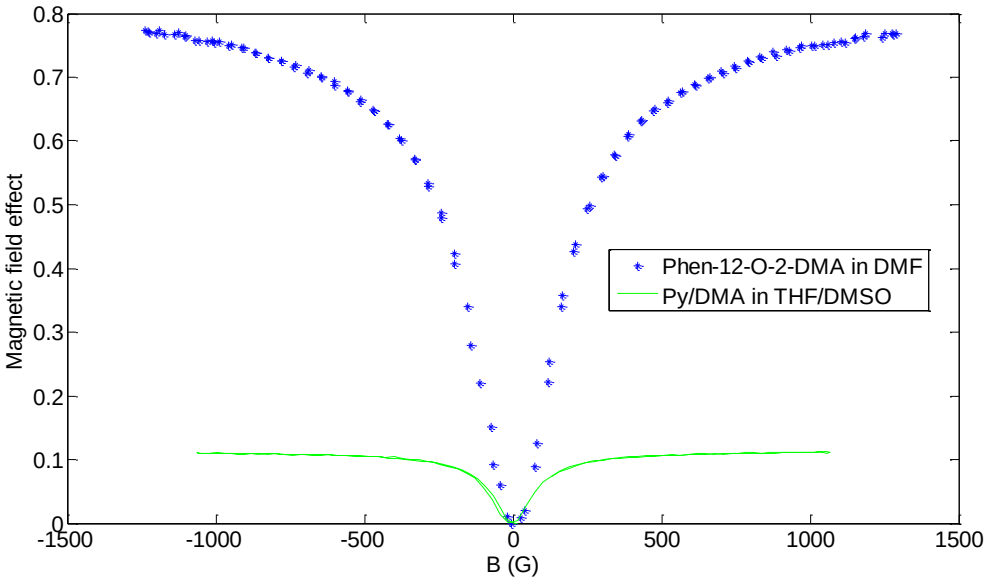

Fig. 5.1 MFE comparison between unlinked Py/DMA in a solvent mixture of THF/DMF and Phen-12-O-2-DMA in DMF

The fluorescence emission spectra of high applied field vs. no applied field for all three molecules are shown in Fig. 5.2. The excitation wavelengths are chosen to be the absorption peak of each compound and the solvents are chosen to maximize MFE. The shorter wavelength fluorophore fluorescence comes from direct relaxation of the excited state of the acceptor. Since it does not go through a radical pair intermediate, the

magnetic field has no effect on the direct fluorescence, but increases the exciplex fluorescence at longer wavelength. This is clearly illustrated in Fig. 5.3 which plots the MFE as a function of emission wavelength.

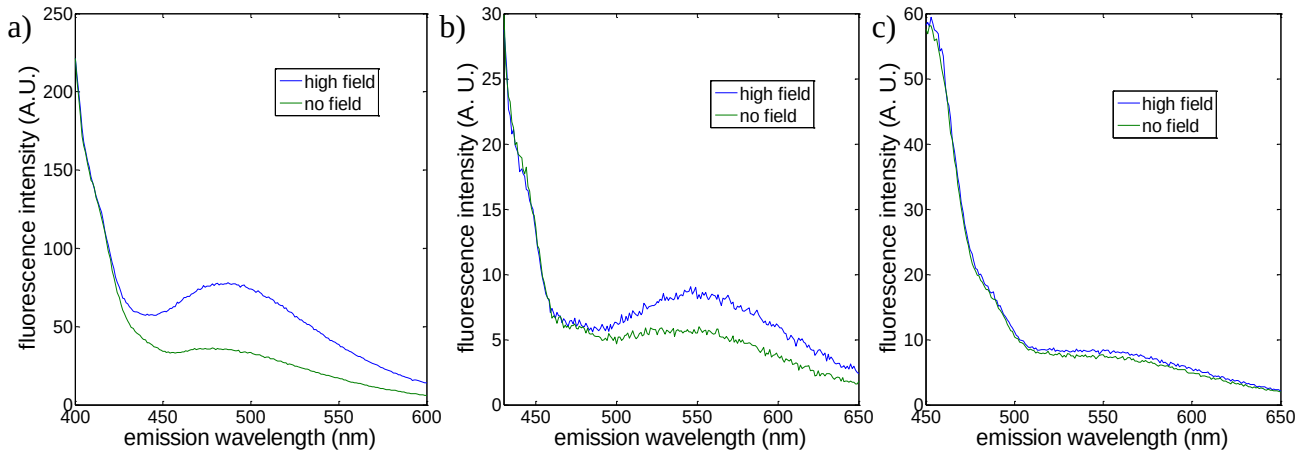

Fig. 5.2 MFE as a function of emission wavelength, the blue and green curves are fluorescence intensity with high field and no field applied, respectively. The excitation wavelengths for each compound are chosen to maximize MFE a) phen-12-O-2-DMA in DMF, excitation wavelength 308nm b) pyrene-12-O-2-DMA in DMF, excitation wavelength 346nm c) anthracene-12-O-2-DMA in 40% THF / 60% acetone, excitation wavelength 405nm

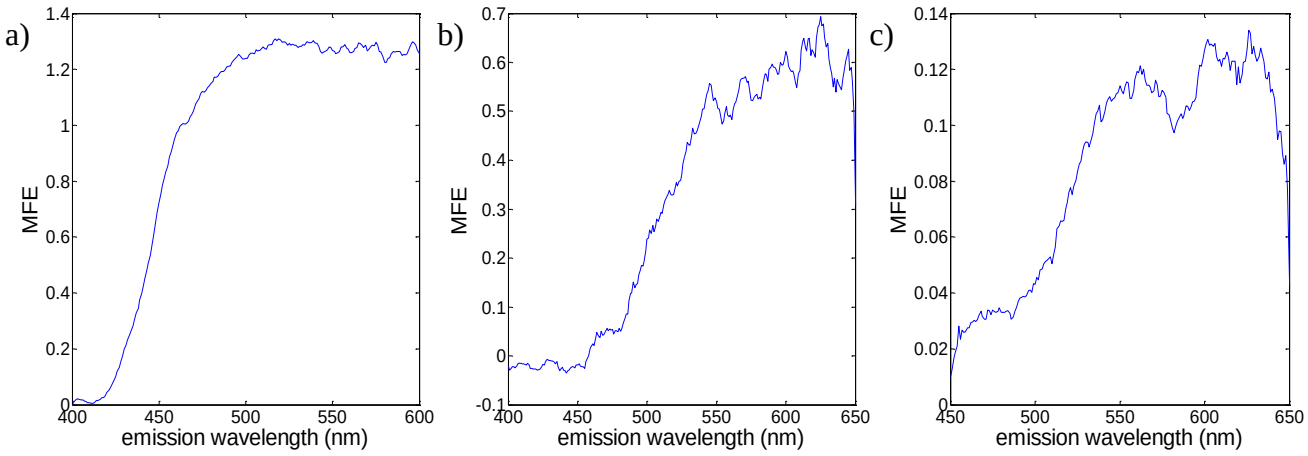

Fig. 5.3 MFE as a function of emission wavelength, a) phen-12-O-2-DMA b) pyrene-12-O-2-DMA c) anthracene-12-O-2-DMA, the conditions are the same as in Fig. 5.2, MFE is defined as $\Delta F / F(B=0)$

Fixing the emission filter to be around the peak exciplex fluorescence, we also measured the MFE signal for the three compounds as a function of excitation wavelength. The results are shown in Fig. 5.4. In general the MFE is largest at the peak absorption wavelength. The phenanthrene, pyrene and anthracene compounds have maximum MFE of 130%, 60%, and 12% respectively. The peak absorption wavelength increases as the MFE on fluorescence decreases; they are 308 nm, 346 nm, and 405 nm, for the three compounds respectively. Anthracene-12-O-2-DMA displays significant MFE with excitation in the visible, which is a very desirable quality. The drawback for this molecule is the low ratio of exciplex fluorescence to prompt fluorescence. Shortening the linker between the donor and acceptor increases the efficiency of electron transfer and exciplex formation. We synthesized a shorter version of the compound: anthracene-8-O-

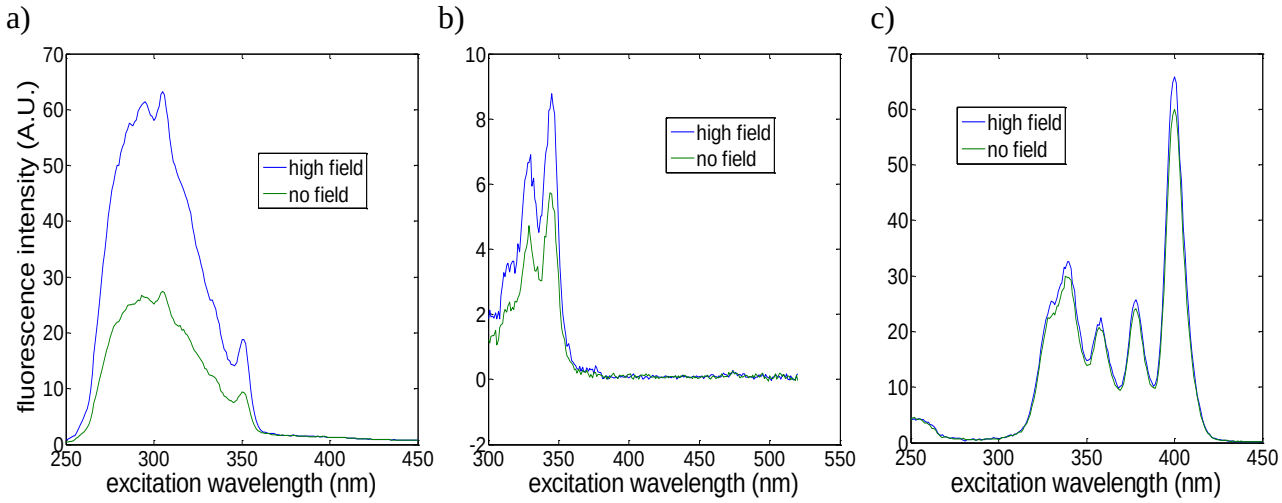

Fig. 5.4 MFE as a function of excitation wavelength, the blue and green curves are fluorescence intensity with high field and no field applied, respectively. The emission wavelengths are chosen to be the exciplex fluorescence peak for each compound a) phen-12-O-2-DMA in DMF, emission wavelength 525 nm b) pyrene-12-O-2-DMA in DMF, emission wavelength 550 nm c) anthracene-12-O-2-DMA in 40% THF / 60% acetone, emission wavelength 550 nm

2-DMA. However, this molecule needs UV excitation to display MFE on the order of 10%.

We pay particular attention to the phenanthrene compound which displays the largest MFE. Fig. 5.5a) shows MFE as a function of excitation wavelength. MFE is as high as 130% at around 308 nm, and drops to about 80% at 355 nm. For transient measurements we are restricted to excite at 355 nm as that is the pulsed source we have available. In Fig. 5.5b) we compare the fluorescence emission curves at these two different excitation wavelengths. High field is applied and the curve is normalized by the fluorescence intensity at 400 nm. They have different shapes which suggest there are different excited states; some are more likely to be excited by shorter wavelength. Excitation at 308 nm produces a higher proportion of red-shifted exciplex fluorescence. Since MFE is larger at longer emission wavelength, this is likely to be the source of the

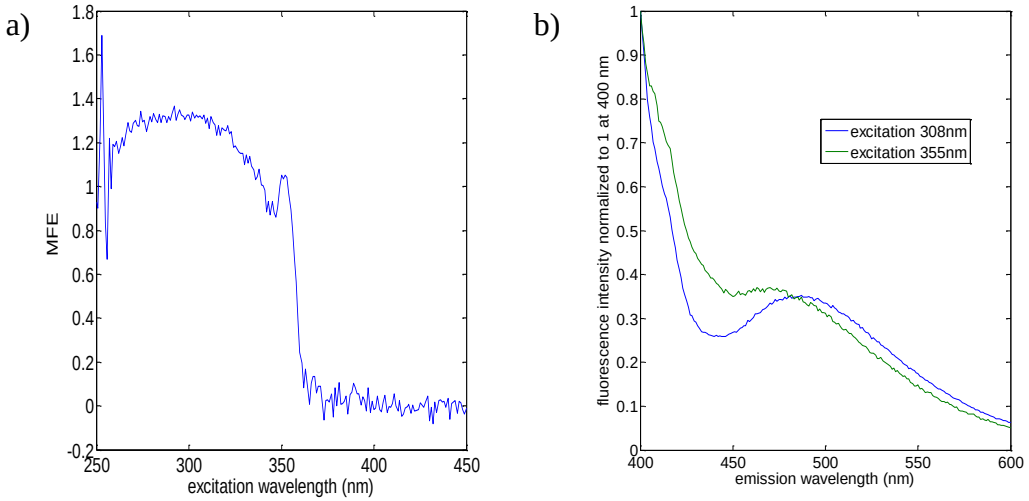

Fig. 5.5 a) MFE of phen-12-O-2-DMA as a function of excitation wavelength b) fluorescence emission curves with high magnetic field at two different excitation wavelengths, normalized to fluorescence intensity at 400 nm

difference in MFE of the two excitation wavelengths.

5.2 Transient fluorescence measurements

We have also measured the magnetic field effect on transient fluorescence of the chained compounds. The sample cuvettes are excited with an Nd-YAG pulsed laser operating at 355 nm (Spectra-Physics quanta-ray). The pulse width is 5 ns. The fluorescence is collected from the bottom of the cuvette and directed through a light guide onto a PMT (Hamamatsu HF11526-20-NF). High (1500 G) and zero magnetic fields are alternatively applied to the sample by an electromagnet. The output from the PMT is recorded and averaged on an oscilloscope (Tektronix TDS 2024B).

The results for phen-12-O-2-DMA are shown in fig. 5.6. A total of 320 pulses are averaged to produce each trace. We plot the time resolved fluorescence under high field

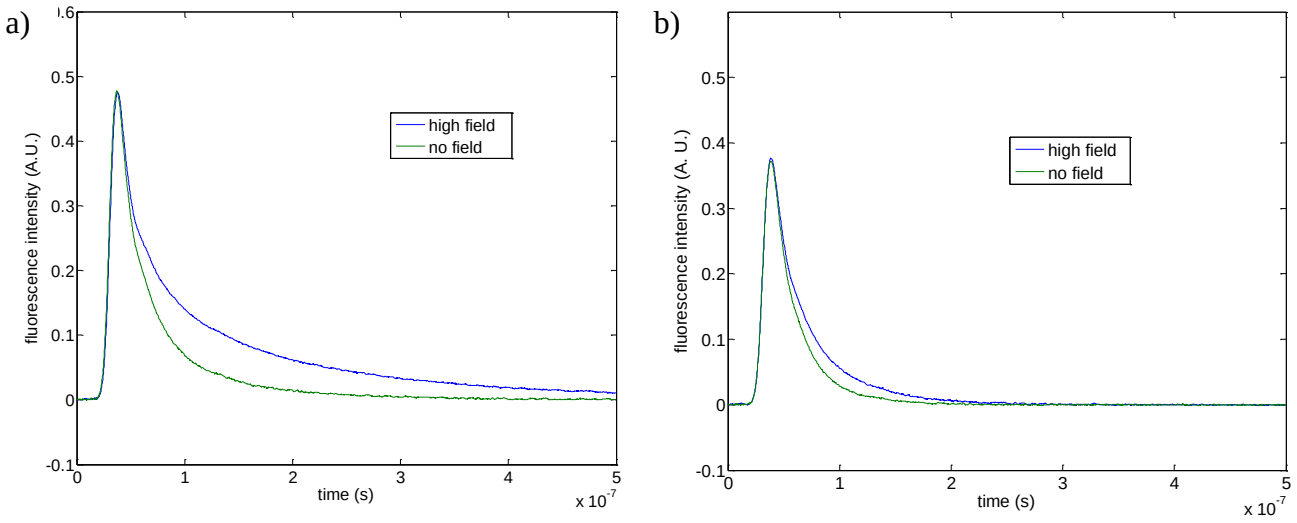

Fig. 5.6 Transient fluorescence measurements on phen-12-O-2-DMA a) The sample is degassed by purging with N2 gas. b) The sample is not purged

and no field conditions, for samples that have been purged with N2 gas to remove oxygen and not purged. At zero field, the fluorescence intensity of the purged sample is about 67% higher than the unpurged sample. The MFE is 79% and 26% for the purged and unpurged samples, respectively. This illustrates the strong quenching of the radical state by oxygen.

Similar to unchained systems, the effect of solvent on MFE is also significant for the chained compounds. In fig. 5.7, we compare the transient fluorescence measurements of pyrene-12-O-2-DMA in two different solvents. On the left we have DMF. On the right we have 25% DMF and 75% THF, which has a much lower dielectric constant than pure DMF. After the electron transfer, the donor and acceptor are oppositely charged. High dielectric constant of DMF provides effective shielding of the Coulomb attractive force. Therefore the donor / acceptor pair diffuses farther apart from each other. Longer distance reduces the effect of exchange interaction and allows more effective intersystem crossing. This leads to larger MFE as intersystem crossing is the step affected by external magnetic field. Longer separation also reduces fluorescence intensity as the molecule is more likely to be quenched non-radiatively.

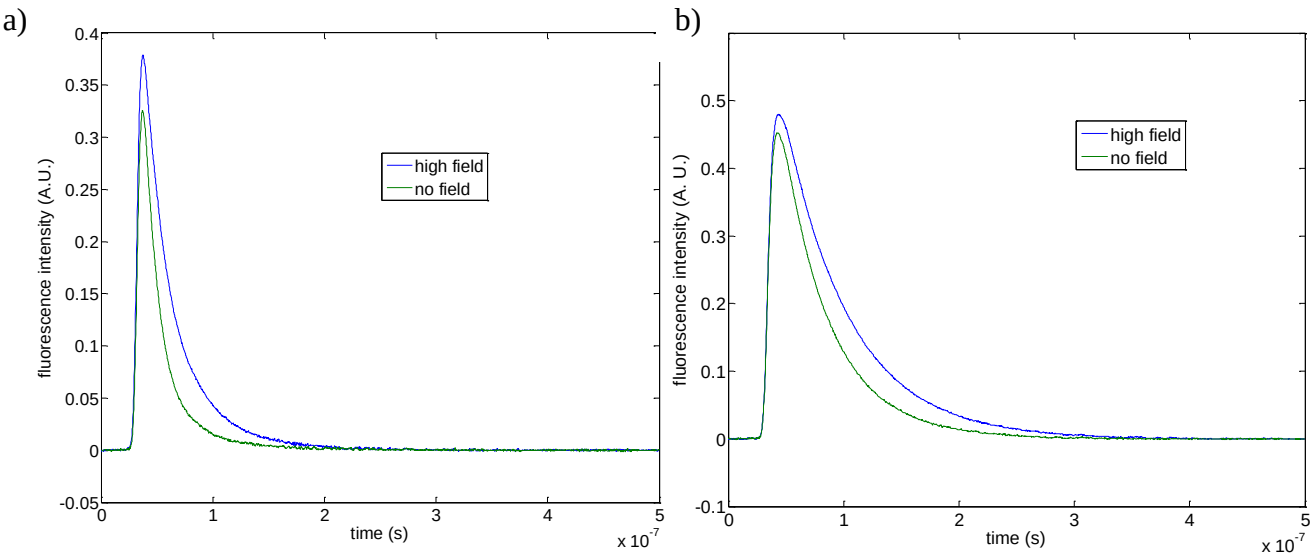

Fig. 5.7 Transient fluorescence measurements on pyrene-12-O-2-DMA a) The solvent is DMF b) The solvent is 25% DMF and 75% THF

5.3 Transient absorption measurements

Steady state and transient fluorescence measurements allow us to observe the signal from recombination of the radical pair in the singlet state. If the spin state is triplet at reencountering, there could be an electron back transfer to create triplet states of the acceptor. In unchained systems, we can observe the signal from the triplet states from delayed fluorescence. The triplet species also have different absorption spectra from the ground or singlet states. We observe these triplet states in the chained compounds directly by measuring transient absorption. The excitation source is Nd-YAG pulsed laser at 355 nm (Spectra-Physics quanta-ray). The probe beam is aligned to be nearly collinear with the excitation pulse and detect on a photodiode. The signal is fed to and averaged by an oscilloscope (Tektronix TDS 2024B). Electromagnet is used to alternatively apply high field (1500 G) and no field. For the probe laser we first use a supercontinuum laser (Fianium SC-450) and acousto-optic tunable filter (AOTF) to scan through various

wavelengths in the visible range to identify the approximate locations of the absorption peak. Then we use various single wavelength lasers with the suitable wavelength for each compound, as these lasers are more stable and provide higher power.

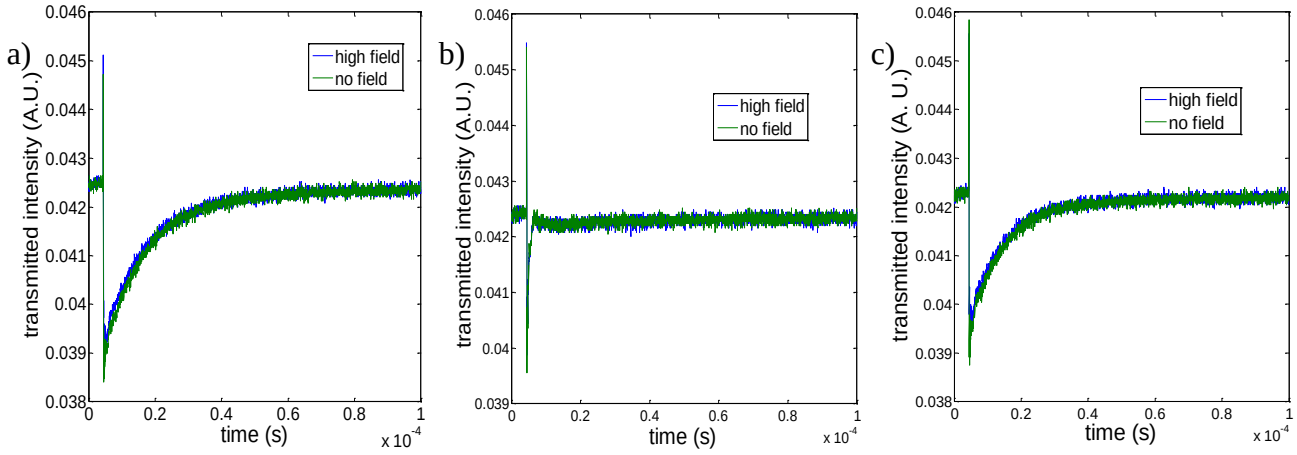

Fig. 5.8 Transient absorption measurement of phen-12-O-2-DMA with probe laser at 488 nm a), the sample is degassed by purging with N2 gas b) the sample is opened to air, oxygen comes into the solution c) the same sample is degassed again

The triplet states should have the following properties: very sensitive to the presence of oxygen, much longer lifetime compared to the prompt fluorescence when oxygen is removed, display MFE that have the opposite sign to prompt fluorescence because the triplet population is reduced when intersystem crossing is suppressed. These properties are demonstrated in the measurement of phen-12-O-2-DMA in fig. 5.8. Fig 5.8a) shows the signal from a degassed sample. The absorbing species has a lifetime on the order of 10 μs, which is two orders of magnitude larger than the transient fluorescence signal. In b), the sample is opened to air, and the transient absorption signal mostly disappeared as the lifetime of the triplet states is shortened by the presence of oxygen. When the same sample is re-degassed, the signal comes back. This high

sensitivity to oxygen suggests that we are observing absorption by triplet states. Opposite to normal MFE on fluorescence, application of magnetic field reduces the signal. For phen-12-O-2-DMA, the MFE on triplet absorption is 8%. We show similar measurements on pyrene-12-O-2-DMA and anthracene-12-O-2-DMA in fig. 5.9. The MFE for them are 11% and 26%, respectively.

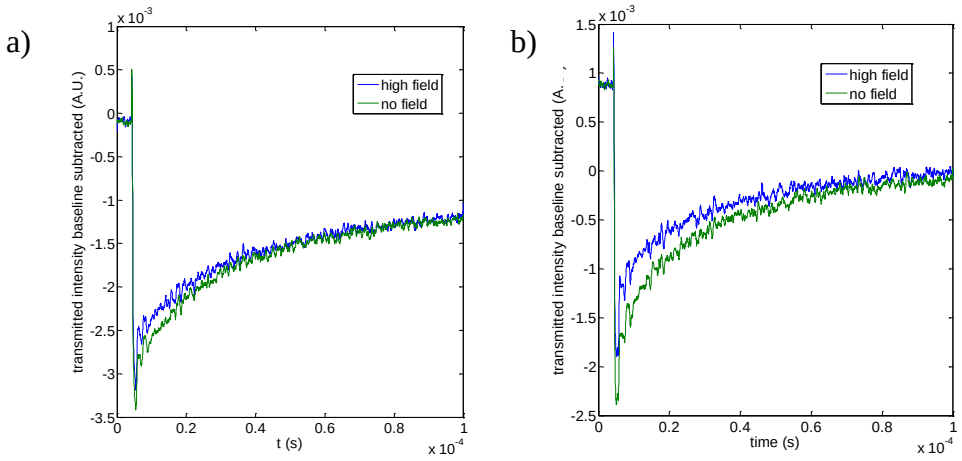

Fig. 5.9 Transient absorption measurements on pyrene-12-O-2-DMA and anthracene-12-O-2-DMA a) pyrene-12-O-2-DMA, probe wavelength 447nm, MFE: 11% b) anthracene-12-O-2-DMA, probe wavelength 447nm, MFE: 26%

5.4 Discussion

We compare the MFE measurements on the three chained compounds in Table 5.1. We can observe two trends. The strength of MFE on singlet fluorescence is high for molecules that show a smaller MFE on triplet absorption and absorb higher energy photons. These trends can be explained as follows. In the absence of external magnetic field, the excited system has a certain branching ratio between singlet and triplet states. Photoexcitation generates singlet and triplet in the ratio of s/(1-s). Application of magnetic field increases the singlet branching ratio s by Δs. The MFE on singlet and

triplet populations are then Δs/s and -Δs/(1-s), respectively. Therefore for compounds with a small s under no field, MFE will be large for singlet fluorescence and small for triplet absorption, and vice versa for compounds with a large s. This is why the MFE on these two channels are opposite in sign and their magnitudes are negatively correlated. This is the same explanation for why MFE on delayed fluorescence has the opposite sign to prompt fluorescence.

Table 5.1 Comparison of the MFE signals of three chained compounds

	MFE on fluorescence (singlet)	MFE on transient absorption (triplet)	Absorption peak	Quantum Yield
phenanthrene	130%	8%	308 nm	0.20
pyrene	60%	11%	346 nm	0.27
anthracene	12%	26%	405 nm	0.58

The energy of a radical pair that is oppositely charged increases with separation distance due to Coulomb interaction. Therefore the energy of photon absorbed could be positively correlated with average separation distance of radical pairs generated. Longer separation reduces the effect of exchange interaction and allows more effective intersystem crossing. This leads to a lower singlet branching ratio s, greater effect due to external field, therefore a higher Δs. As a result, compounds that absorb at higher energy show a larger MFE on fluorescence.

We find further evidence for this interpretation in measurements of the quantum yields of the three molecules measured at their respective absorption peaks. The data is summarized in the last column in Table 5.1. To obtain the quantum yield we first measured the total fluorescence intensity including both prompt and exciplex

fluorescence. We then compared to a R6G sample in water with known quantum yield of 0.95, and arrived at the final results with correction for the spectra of the excitation source and the detector. A high quantum yield indicates a high percentage of radiative decay and correspondingly a low rate of non-radiative decay. Exciplex fluorescence and triplet absorption are parts of radiative and non-radiative decay, respectively. Therefore for a molecule that shows a small MFE on exciplex fluorescence, we expect large fluorescence intensity, and higher quantum yield. This is the trend we observe in the data.

The results suggest that molecules with shorter absorption wavelength are more likely to display larger MFE. This could also be the reason that it is difficult to identify systems that absorb in the visible and show MFE on fluorescence. Furthermore, systems with large MFE on the singlet channel do not necessarily have large MFE on the triplet channel. They can in fact be negatively correlated, and the determining factor is the singlet to triplet ratio in absence of external field. High singlet to triplet ratio favors larger MFE on the triplet channel, and lower ratio favors larger MFE on the singlet channel. These results suggest potential directions for engineering molecular systems toward desired properties with respect to MFE.

Chapter 6. Local geometry of electromagnetic waves and its role in molecular multipole transitions

The earlier chapters describe studies of magnetic fields, and this chapter presents our work on optical fields. This chapter is based on ref. [83]. We study the response of a small molecule to monochromatic fields of arbitrary three-dimensional geometry. First, we consider the allowed configurations of the fields and field gradients at a single point in space. Many configurations cannot be generated from a single plane wave, regardless of polarization, but any allowed configuration can be generated by superposition of multiple plane waves. There is no local configuration of the fields and gradients that *requires* near-field effects. Second, we derive a set of local electromagnetic quantities, where each couples to a particular multipole transition. These quantities are small or zero in plane waves, but can be large in regions of certain superpositions of plane waves. Our findings provide a systematic framework for designing far-field and near-field experiments to drive multipole transitions. The proposed experiments provide information on molecular structure that is inaccessible to other spectroscopic techniques, and open the possibility for new types of optical control of molecules.

6.1. Introduction

Propagating plane waves comprise only a minute fraction of all solutions to Maxwell's Equations. Fields with sinusoidal time dependence but with more complex spatial variation routinely arise in the context of multiple-wave interference and optical

near fields. These variously shaped fields can excite molecular multipole transitions that are tickled weakly—if at all—by far-field plane waves. Here we study the geometry of non-plane-wave electromagnetic fields, and the linear interaction of these fields with small molecules. For each type of multipole transition we present a local electromagnetic quantity that determines the strength of the coupling to that transition. We propose simple field configurations and spectroscopic techniques that selectively probe particular multipole transitions.

For most molecules, far-field plane waves couple weakly to molecular multipole transitions beyond electric dipole, and in some cases the coupling is identically zero. Weak coupling beyond electric dipole arises because the wavelength of light is typically much larger than molecular dimensions. Higher multipole transitions are excited more weakly than electric dipole by powers of (a/λ), where a is the molecular size and λ is the wavelength. Additionally, excitation of some multipole transitions by plane waves is identically zero due to the definite relations among electric fields, electric field gradients and magnetic fields that arise in all plane waves. These transitions vanish for plane waves regardless of the wavelength, polarization, or degree of orientation of the molecules.

Steeply varying fields are widespread in Nature. They play a particularly important role in intermolecular interactions because the electromagnetic field due to one molecule may be highly nonuniform over the extent of its neighbor. These field gradients couple to multipole transitions beyond electric dipole that are important in mediating intermolecular energy transfer[84], intermolecular forces[85], and chemical

reactions[86]. To understand these processes[87,88], one would like to explore the response of a test molecule to a variety of time-harmonic electric fields, magnetic fields, and field gradients.

Metallic nanostructures, photonic crystals, and metamaterials also generate local fields that are highly contorted. Surface-enhanced optical effects are well known for molecules near metal surfaces[89,90], and include enhanced fluorescence[91], Raman scattering[92], two-photon excitation[93], and photochemistry[94]. These phenomena are typically interpreted in terms of enhancement of the electric field strength alone[89]; but the relative magnitude and direction of electric and magnetic fields and their gradients near a nanostructure need not correspond with their values in a plane wave, and can thereby violate far-field selection rules. For instance, it was recently predicted that magnetic nanostructures can dramatically enhance the rate of intersystem crossing in nearby molecules through interaction of magnetic gradients with a magnetic quadrupole transition in a radical pair[14]. Nanostructures can sculpt the fields to bring "forbidden" transitions to light.

Thus it is interesting to study the response of molecules to non-plane-wave electromagnetic fields. In section 2 we study the possible local geometries of monochromatic fields allowed by Maxwell's Equations. There are many valid field configurations that cannot be produced by a monochromatic plane wave. This distinction between the space of possible fields, and the space of plane wave fields is an important aspect of spectroscopy that has not received adequate attention.

We show that *any* valid configuration of electric and magnetic fields and field gradients can be created at discrete points in space by superposition of up to 32 linearly

polarized monochromatic plane waves. Thus, while it may be convenient to use nanostructures or near-field optics to generate certain field configurations, these tools are not strictly necessary.

Next we ask: What attributes of the field should one calculate to determine the rate of excitation of a particular multipole transition? Our group previously considered this question in the context of randomly oriented chiral molecules and circular dichroism. We introduced a time-even pseudoscalar that measures the local handedness of the electric and magnetic fields:

$$C \equiv \frac{\varepsilon_0}{2} \vec{E} \cdot \nabla \times \vec{E} + \frac{1}{2\mu_0} \vec{B} \cdot \nabla \times \vec{B} . \tag{6.1}$$

This "Optical Chirality" determines the dissymmetry in the rate of excitation of a small chiral molecule[95].

In section 3 we study how other bilinear field objects couple to other kinds of multipole transitions. In section 3.2 we treat the coupling of electric field gradients to electric dipole-electric quadrupole (E1-E2) transitions. These transitions average to zero for randomly oriented molecules, regardless of the field geometry. Near an interface, however, molecules may have a uniaxial orientation, leading to several interface-selective signals for appropriately sculpted fields.

In Section 3.3 we also treat electric dipole-magnetic dipole (E1-M1) transitions. Upon orientational averaging, these transitions survive only for chiral molecules and chiral fields. For uniaxially oriented molecules, however, E1-M1 transitions combine with E1-E2 transitions to give an interface-selective signal for appropriately sculpted

fields. Remarkably, many of these transitions are completely invisible to plane waves, but become visible in a standing wave.

In sections 3.4-3.6, we construct simple standing wave fields which selectively excite E1-E2 and E1-M1 transitions in localized regions of space. We propose a remarkably simple experiment to test these predictions.

In section 4 we consider magnetic circular dichroism (MCD) as a perturbation to the electric dipole transition. We derive the electromagnetic quantity that couples to MCD and propose an experiment in which a focused beam of *linearly* polarized light probes the same molecular quantities that are usually probed with circularly polarized light in MCD.

In 1964 Lipkin introduced ten conserved electromagnetic quantities that are quadratic in the fields, which he called the "Zilch".[96] He and subsequent workers failed to find any physical meaning for the Zilch.[97,98] One of these, termed Z^{000}, is the same as the optical chirality we previously introduced. In section 5 we show that six of the remaining Lipkin terms are the EM quantities that couple to E1-M1 transitions, and the other three couple to molecules in DC magnetic fields. We present a protocol for generating an arbitrary number of conserved Lipkin-like quantities.

6.2 Allowable monochromatic fields

How much freedom do Maxwell's Equations give us to sculpt electromagnetic fields? A small molecule is only sensitive to local fields and field gradients, so we restrict attention to these aspects of the field about a fixed point in space, chosen to lie at

the origin **r** = 0. A related question is: can we generate any allowed field configuration using combinations of plane waves, or are there configurations that only arise in optical near-fields? We show, perhaps contrary to intuition, that *any* time-harmonic local field configuration can be generated by superposition of propagating plane waves.

The most general monochromatic electric field follows an elliptical trajectory, with arbitrary orientation, amplitude, ellipticity, and phase. It is mathematically convenient to describe this configuration by the real part of

$$\tilde{\mathbf{E}} = \tilde{\mathbf{E}}^{(0)} e^{-i\omega t}, \tag{6.2}$$

where $\tilde{\mathbf{E}}$ and $\tilde{\mathbf{E}}^{(0)}$ are complex vectors. We use symbols without tilde to represent physical quantities, which are the real parts of the corresponding complex terms. A single propagating plane wave can generate any desired electric field ellipse. One simply chooses the polarization, amplitude, and direction of propagation of the wave.

Within the electric point-dipole approximation (PDA), the local electric field is the only quantity needed to describe the interaction of light with matter. In this case plane waves span the space of relevant fields, so the distinction between plane waves and other fields is moot. However, if one considers multipole transitions beyond electric dipole, then the magnetic field and the electric and magnetic field gradients become important. In this case we find allowable field configurations that cannot be produced by a single plane wave.

One can imagine a monochromatic field configuration that at a single point consists of an electric field ellipse and a magnetic field ellipse, each with arbitrary amplitude, ellipticity, orientation, and phase (Fig. 6.1). This configuration is consistent

with Maxwell's Equations, but unless **E** and **B** are always perpendicular, it does not occur in a plane wave. First we show by explicit construction how to generate this configuration by combination of multiple standing waves. Then we use an algebraic approach to show that any electric and magnetic field *gradients* allowed by Maxwell's

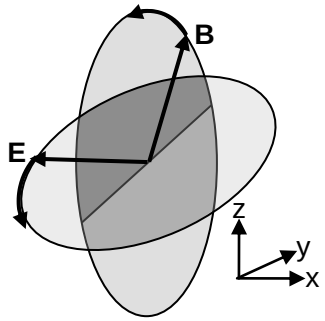

Fig. 6.1. Arbitrary electric and magnetic ellipses at a single point in space. This configuration cannot occur in a plane wave, but can occur in a combination of two standing waves.

Equations can be superimposed on these ellipses by addition of more plane waves.

Consider a standing wave composed of counterpropagating plane waves, linearly polarized in the same plane. At the electric anti-nodes, the magnetic field is zero, and *vice versa*. By overlapping the electric anti-nodes of two such standing waves, with different linear polarizations, phases, and propagation axes, one creates an arbitrary electric field ellipse at a point where the magnetic field is zero. By combining the magnetic anti-nodes of two more standing waves in a similar manner, one creates an arbitrary magnetic ellipse where the electric field is zero. Finally, one superimposes the electric ellipse with the magnetic ellipse, to achieve the arbitrary field configuration shown in Fig. 6.1. We describe the state of the field in Fig 6.1 by a six-element complex vector, $\left(\tilde{\mathbf{E}},\tilde{\mathbf{B}}\right)$.

Now we consider the electric and magnetic field gradients. The electric gradient $\nabla\tilde{\mathbf{E}}$ has nine components $\tilde{E}_{\beta\gamma}$, indicating the derivative of $\tilde{E}_{\beta}$ in the γ direction. The magnetic gradient also has nine components. Once we have determined the vector $\left(\tilde{\mathbf{E}},\tilde{\mathbf{B}}\right)$, Maxwell's Equations set the divergence and curl of $\tilde{\mathbf{E}}$ and $\tilde{\mathbf{B}}$, leaving us with five independent components for $\tilde{E}_{\beta\gamma}$ and five for $\tilde{B}_{\beta\gamma}$. Thus we have 6 independent components for the fields, and 10 for the gradients. We describe the complete field geometry at a single point by a vector, $\tilde{\mathbf{Q}} \equiv \left(\tilde{\mathbf{E}},\tilde{\mathbf{B}},\nabla\tilde{\mathbf{E}},\nabla\tilde{\mathbf{B}}\right)$, with 16 independent complex components.

Now the question is: can any value of $\tilde{\mathbf{Q}}$ be created by superposition of linearly polarized plane waves? Every plane wave contributes to $\tilde{\mathbf{E}}$, $\tilde{\mathbf{B}}$, $\nabla\tilde{\mathbf{E}}$, and $\nabla\tilde{\mathbf{B}}$, and at a single point in space the wave can be represented as a vector in the space of $\tilde{\mathbf{Q}}$. If we can find a set of plane waves that span the space of $\tilde{\mathbf{Q}}$, then the problem is solved.

To construct a basis set for $\tilde{\mathbf{Q}}$, we restrict attention to linearly polarized, monochromatic plane waves, each with fixed wavevector and polarization, but variable amplitude. These are of the form:

$$\tilde{\mathbf{E}} = \mathbf{E}^{(0)} \exp(i\mathbf{k}\cdot\mathbf{r} - i\omega t)\exp(i\phi)$$

$$\tilde{\mathbf{B}} = \frac{1}{c}\hat{\mathbf{k}}\times\tilde{\mathbf{E}}$$

$$\tilde{E}_{\beta\gamma} = iE_{\beta}^{(0)}k_{\gamma}\exp(i\mathbf{k}\cdot\mathbf{r} - i\omega t)\exp(i\phi)$$

$$\tilde{B}_{\beta\gamma} = iB_{\beta}^{(0)} k_{\gamma} \exp(i\mathbf{k}\cdot\mathbf{r} - i\omega t)\exp(i\phi) \tag{6.3}$$

with $\mathbf{E}^{(0)}$ and $\mathbf{k}$ real. We have the constraints:

$$\mathbf{E}^{(0)} \cdot \mathbf{k} = 0, \tag{6.4}$$

$$|\,\mathbf{k}\,| = k_0 . \tag{6.5}$$

For each plane wave we evaluate its contribution to $\tilde{\mathbf{Q}}$ at the origin. In Table 1 of Appendix 1 we list 16 monochromatic plane waves with $\phi = 0$ which span the real part of $\tilde{\mathbf{Q}}$. The same 16 waves with $\phi = \pi/2$ span the imaginary part of $\tilde{\mathbf{Q}}$.

Thus it is possible, using only plane waves, to achieve an arbitrary configuration of EM fields and gradients at a point in space. Nanostructures and near-field optics may offer practical advantages for the creation of these fields, but these tools are not strictly necessary. We now consider the response of a molecule to a field with an arbitrary value of $\tilde{\mathbf{Q}}$.

6.3 Molecular Multipole Transitions

6.3.1 Induced oscillating molecular multipoles.

A molecule subjected to a time-harmonic EM field develops time-harmonic charge and current distributions, which may be described by a multipole expansion:[99]

$$\begin{aligned} \tilde{\mu}_{\alpha} &= \tilde{\alpha}_{\alpha\beta}\tilde{E}_{\beta} + \frac{1}{3}\tilde{A}_{\alpha\beta\gamma}\tilde{E}_{\beta\gamma} + \tilde{G}_{\alpha\beta}\tilde{B}_{\beta} \\ \tilde{\theta}_{\alpha\beta} &= \tilde{a}_{\gamma\alpha\beta}\tilde{E}_{\gamma} + \ldots \\ \tilde{m}_{\alpha} &= \tilde{g}_{\alpha\beta}\tilde{E}_{\beta} + \ldots \end{aligned} \quad , \tag{6.6}$$

where α, β, γ are Cartesian indices, and $\tilde{\mu}$, $\tilde{\theta}$, $\tilde{m}$ are the oscillating electric dipole, electric quadrupole and magnetic dipole, respectively. The quantity $\tilde{\alpha}_{\alpha\beta}$ is the dynamic electric dipole polarizability, $\tilde{A}_{\alpha\beta\gamma}$ and $\tilde{a}_{\gamma\alpha\beta}$ are the mixed electric dipole-quadrupole polarizabilities, and $\tilde{G}_{\alpha\beta}$ and $\tilde{g}_{\alpha\beta}$ are the mixed electric-magnetic dipole analogues. We use the Einstein summation convention in which repeated Cartesian indices are summed.

The transition matrix elements and the lineshape functions are each, in general, complex. The polarizability tensors such as $\tilde{A}_{\alpha\beta\gamma}$ and $\tilde{G}_{\alpha\beta}$ are products of matrix elements and lineshapes, so these are generally complex too. In the absence of a DC magnetic field, the dynamics respect time-reversal symmetry, and all molecular eigenfunctions can be chosen to be real[100]. In this case electric dipole and electric quadrupole transition matrix elements are purely real, and magnetic dipole transition matrix elements are purely imaginary. From the perturbation theory expressions for the molecular response tensors one can show that:

$$\begin{aligned} \tilde{A}_{\alpha\beta\gamma} &= \tilde{a}_{\gamma\alpha\beta} = A'_{\alpha\beta\gamma} + iA''_{\alpha\beta\gamma} \\ \tilde{G}_{\alpha\beta} &= -\tilde{g}_{\alpha\beta} = G'_{\alpha\beta} + iG''_{\alpha\beta} \end{aligned} \tag{6.7}$$

where $A'_{\alpha\beta\gamma}$, $A''_{\alpha\beta\gamma}$, $G'_{\alpha\beta}$ and $G''_{\alpha\beta}$ are real frequency-dependent functions. Note that we use a different notation from Barron[99] because we are restricting attention to conditions where the molecular eigenfunctions can be chosen to be real.

The induced multipoles absorb energy from the fields at an average rate

$$\Gamma = \left\langle E_\alpha \dot{\mu}_\alpha + \frac{1}{3} E_{\alpha\beta} \dot{\theta}_{\alpha\beta} + B_\alpha \dot{m}_\alpha + ... \right\rangle_t , \tag{6.8}$$

where $\langle\ \rangle_t$ indicates an average over time. Substitution of Eq. 6.6.6 into Eq. 6.6.8 leads to an expression for the rate of absorption in terms of molecular properties and local EM fields. This expression contains many terms, each of which is a product of a molecular tensor component and two field quantities.

Each term is responsible for a spectroscopic observable. We classify these observables by the field components that contribute. For instance, if we express the electric field as in Eq. 6.6.2, then the first term in the expansion is

$$\Gamma_{E1-E1} = \omega\alpha''_{\alpha\beta}E^{(0)}_{\alpha}E^{(0)}_{\beta}, \tag{6.9}$$

which is responsible for the pure electric dipole absorption which usually dominates. We neglect terms of order M2 and higher, because these are negligibly small for most molecules.

In non-plane wave geometries, the relative strengths of the field quantities can be adjusted to enhance the contribution of particular molecular terms. This flexibility enables enhanced spectroscopy with sculpted fields, and in some cases gives rise to observables not probed by plane waves.

6.3.2 Electric dipole – electric quadrupole (E1-E2) excitation

Two effects contribute to E1-E2 transitions: (1) interaction of the electric field with dipole moments induced by the field gradient and (2) interaction of the field gradient with quadrupole moments induced by the electric field. We now treat each in turn.

The complex fields at the origin $\tilde{E}_\beta = \tilde{E}_\beta^{(0)} e^{-i\omega t}$, $\tilde{E}_{\beta\gamma} = \tilde{E}_{\beta\gamma}^{(0)} e^{-i\omega t}$, can be expressed as

$$\begin{aligned} \tilde{E}_\beta &= E_\beta + \frac{i}{\omega}\dot{E}_\beta \\ \tilde{E}_{\beta\gamma} &= E_{\beta\gamma} + \frac{i}{\omega}\dot{E}_{\beta\gamma} \end{aligned}, \tag{6.10}$$

where E_β and $E_{\beta\gamma}$ are the real oscillating field components. The electric dipole moment induced by an electric field gradient is given by combining Eqs. 6.6 and 6.10:

$$\tilde{\mu}_\alpha = \frac{1}{3}(A'_{\alpha\beta\gamma} + iA''_{\alpha\beta\gamma})\left(E_{\beta\gamma} + \frac{i}{\omega}\dot{E}_{\beta\gamma}\right). \tag{6.11}$$

The time-dependent absorption rate due to this interaction is:

$$E_\alpha \dot{\mu}_\alpha = \frac{1}{3}A'_{\alpha\beta\gamma}E_\alpha \dot{E}_{\beta\gamma} + \frac{\omega}{3}A''_{\alpha\beta\gamma}E_\alpha E_{\beta\gamma} \tag{6.12}$$

where $\mu_\alpha = \mathrm{Re}(\tilde{\mu}_\alpha)$ is the real component of the complex electric dipole moment; and we used the fact that for time-harmonic fields, $\ddot{E}_{\beta\gamma} = -\omega^2 E_{\beta\gamma}$.

Similarly, the molecular electric quadrupole moment induced by the electric field is:

$$\tilde{\theta}_{\beta\gamma} = (A'_{\alpha\beta\gamma} + iA''_{\alpha\beta\gamma})\left(E_\alpha + \frac{i}{\omega}\dot{E}_\alpha\right), \tag{6.13}$$

where we have used the fact that $\tilde{A}_{\alpha\beta\gamma} = \tilde{a}_{\gamma\alpha\beta}$. The time-dependent absorption rate due to this interaction is

$$\frac{1}{3}E_{\beta\gamma}\dot{\theta}_{\beta\gamma} = \frac{1}{3}A'_{\alpha\beta\gamma}\dot{E}_\alpha E_{\beta\gamma} + \frac{\omega}{3}A''_{\alpha\beta\gamma}E_\alpha E_{\beta\gamma}. \tag{6.14}$$

The total absorption rate is the sum of Eqs. 6.12 and 6.14. The electromagnetic quantity that couples to $A''_{\alpha\beta\gamma}$ is:

$$\frac{2\omega}{3}\left\langle E_\alpha E_{\beta\gamma}\right\rangle_t, \tag{6.15}$$

and the one that couples to $A'_{\alpha\beta\gamma}$ is:

$$\frac{1}{3}\left\langle E_\alpha \dot{E}_{\beta\gamma} + \dot{E}_\alpha E_{\beta\gamma}\right\rangle_t = \frac{1}{3}\left\langle \frac{\partial}{\partial t}(E_\alpha E_{\beta\gamma})\right\rangle_t, \tag{6.16}$$

which vanishes. Thus the rate of the E1-E2 transition is:

$$\Gamma_{E1-E2} = \frac{2\omega}{3} A''_{\alpha\beta\gamma}\left\langle E_\alpha E_{\beta\gamma}\right\rangle_t. \tag{6.17}$$

Terms that couple to $A''_{\alpha\beta\gamma}$ with all three indices distinct give rise to optical activity of oriented molecules[101]. The average of the third rank tensor $\tilde{A}_{\alpha\beta\gamma}$ over all molecular orientations is:

$$\left\langle \tilde{A}_{\alpha\beta\gamma}\right\rangle_\Omega = -\frac{1}{6}\left(\varepsilon_{\alpha\beta\gamma}\tilde{A}_{\alpha\beta\gamma}\right)\vec{\varepsilon}, \tag{6.18}$$

where $\varepsilon_{\alpha\beta\gamma}$ is the third rank isotropic tensor. The tensor components of $\tilde{A}$ are related by $\tilde{A}_{\alpha\beta\gamma} = \tilde{A}_{\alpha\gamma\beta}$,[99] whence $\varepsilon_{\alpha\beta\gamma}\tilde{A}_{\alpha\beta\gamma} = 0$. Therefore the E1-E2 absorption vanishes for unoriented molecules, regardless of the geometry of the EM field.

6.3.3 Electric Dipole - Magnetic Dipole (E1-M1) Transition

Two effects also contribute to E1-M1 transitions: (1) interaction of the electric field with electric dipole moments induced by the magnetic field and (2) interaction of the magnetic field with magnetic dipole moments induced by the electric field. We now treat each in turn.

The magnetic field induces an electric dipole moment according to $\tilde{\mu}_\alpha = \tilde{G}_{\alpha\beta}\tilde{B}_\beta$. By following the same algebra used to derive Eq. 6.6.12, we find that this term contributes a time-dependent absorption rate

$$E_\alpha \dot{\mu}_\alpha = G'_{\alpha\beta} E_\alpha \dot{B}_\beta + \omega G''_{\alpha\beta} E_\alpha B_\beta . \tag{6.19}$$

The electric field induces a magnetic dipole moment according to $\tilde{m}_\beta = \tilde{g}_{\beta\alpha}\tilde{E}_\alpha$. The absorption rate due to this interaction is

$$B_\beta \dot{m}_\beta = -G'_{\alpha\beta} \dot{E}_\alpha B_\beta - \omega G''_{\alpha\beta} E_\alpha B_\beta , \tag{6.20}$$

where we have used the fact that $\tilde{G}_{\alpha\beta} = -\tilde{g}_{\alpha\beta}$. The rates in Eqs. 6.19 and 6.20 are summed to give the total rate of E1-M1 absorption

$$\Gamma_{E1-M1} = G'_{\alpha\beta} \left\langle E_\alpha \dot{B}_\beta - \dot{E}_\alpha B_\beta \right\rangle_t . \tag{6.21}$$

Thus the quantity $\left\langle E_\alpha \dot{B}_\beta - \dot{E}_\alpha B_\beta \right\rangle_t$ determines the rate at which E1-M1 transitions are excited in oriented molecules.

In the case of unoriented molecules, we take the isotropic average and use $\left\langle G'_{\alpha\beta} \right\rangle_\Omega = \frac{1}{3}\left(G'_{\alpha\alpha}\right)\mathbf{I}$, where **I** is the 3-by-3 identity matrix. This quantity is only nonzero

for chiral molecules. Application of Maxwell's Equations in free space to the quantity $\left\langle E_\alpha \dot{B}_\alpha - \dot{E}_\alpha B_\alpha \right\rangle_t$ shows that this object is proportional to Optical Chirality, and is responsible for chiral dissymmetry in the excitation of isotropic molecules.

Higher multipole transitions such as E1-M2, E2-M1, and M1-M1 can be calculated in similar manner. However the molecular response tensors for these transitions tend to be very small, so we deem experimental observation unlikely in the near term.

6.3.4. Multipole transitions in linearly polarized standing waves

Here we demonstrate that a linearly polarized standing wave excites molecular transitions that are invisible to traveling waves. These "achiral multipole transitions" are only detectable for molecules that are uniaxially oriented, and lie within a plane of sub-wavelength thickness. This geometry is common at liquid interfaces, so we propose that achiral multipole transitions can be used for surface-sensitive spectroscopy.

Consider a standing wave composed of two waves counter-propagating along *z* and polarized along *x*. We allow the two waves to have different amplitudes, E_0 and E_0'.

$$\begin{aligned}\tilde{\mathbf{E}}(z,t) &= E_0\hat{\mathbf{e}}_x \exp(i(kz-\omega t)) - E_0'\hat{\mathbf{e}}_x \exp(i(-kz-\omega t)) \\ \tilde{\mathbf{B}}(z,t) &= \frac{E_0}{c}\hat{\mathbf{e}}_y \exp(i(kz-\omega t)) + \frac{E_0'}{c}\hat{\mathbf{e}}_y \exp(i(-kz-\omega t))\end{aligned}. \tag{6.22}$$

The only contribution to E1-E2 absorption is from $E_x E_{xz}$, and the only contribution to E1-M1 absorption is from $E_x \dot{B}_y - \dot{E}_x B_y$. The relevant field objects are:

$$\text{E1-E1:} \qquad \omega\left\langle E_x^2 \right\rangle_t = \frac{\omega}{2}\left[E_0^2 + E_0'^2 - 2E_0E_0'\cos(2kz)\right] \tag{6.23}$$

Achiral E1-E2: $$\frac{2\omega}{3}\left\langle E_x E_{xz}\right\rangle_t = \frac{\omega k}{3} E_0 E_0' \sin(2kz) \tag{6.24}$$

Achiral E1-M1: $$\left\langle E_x \dot{B}_y - \dot{E}_x B_y \right\rangle_t = -kE_0 E_0' \sin(2kz)\,. \tag{6.25}$$

Eq. 6.6.23 determines the spatial dependence of E1-E1 absorption, which is the usual quantity measured in a standing wave. Eqs. 6.24 and 6.25 determine the rates of achiral multipole transitions, and have the remarkable property that they vanish for a plane wave (setting E_0 or E_0' to zero). Achiral multipole transitions are invisible to a single linearly polarized plane wave. We show below that these transitions are also invisible to circularly polarized light, supporting our contention that standing waves can see transitions that plane waves cannot.

Substitution of Eqs. 6.24 and 6.25 into the overall rate of absorption gives

$$\Gamma = \Gamma_{E1-E1} + kE_0 E_0' \sin(2kz)\left(\frac{\omega A_{xxz}''}{3} - G_{xy}'\right). \tag{6.26}$$

The sin(2*kz*) dependence of the achiral multipole transitions combines with the cos(2*kz*) dependence of the E1-E1 transition to create a slight phase shift in the standing wave absorption pattern relative to what would be expected for pure electric dipole absorption.

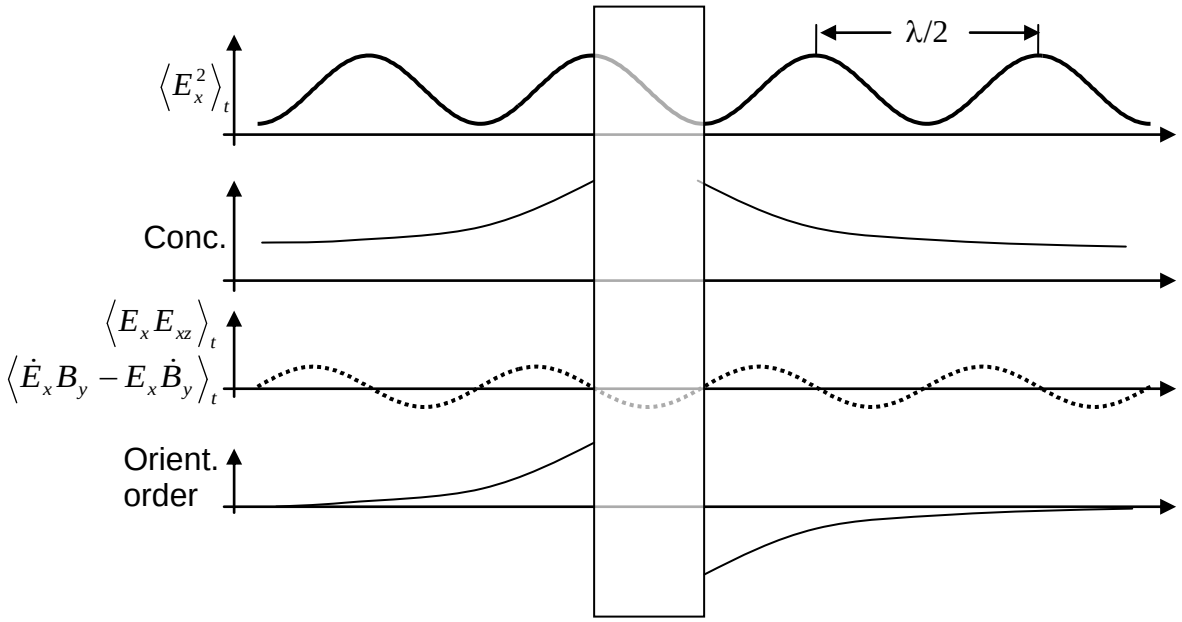

Figure 6.2. Schematic of an experiment to probe achiral E1-E2 and E1-M1 transitions in a liquid. A transparent barrier of thickness $(n/2 + ¼)\lambda$ separates two compartments of liquid and is exposed to a standing wave (for clarity we draw a slab of thickness $\lambda/4$, though this is mechanically implausible). The standing wave is moved perpendicular to the plane of the slab. Molecules may have larger (or smaller) concentration near the interface than in bulk, and may have orientational order near the interface. Only E1-E2 and E1-M1 excitation of the surface-oriented molecules oscillates with translation of the standing wave; the total rate of E1-E1 excitation does not vary.

The consequences of Eq. 6.6.26 vary depending on the degree of orientational order of the molecules. Eq. 6.6.26 applies to perfectly oriented molecules, such as might be found in a crystal. Under isotropic averaging, as in a liquid, $\left\langle \tilde{A}_{\alpha\beta\gamma} \right\rangle_\Omega = 0$, and the off-diagonal components of $\tilde{G}_{\alpha\beta}$ average to zero, even for chiral molecules. Thus these transitions are undetectable in bulk liquid. Near a liquid interface, however, molecules may adopt a uniaxial orientation. A DC electric field can orient molecules too. If the orientation axis coincides with the optical *z*-axis, then we average Eq. 6.6.26 about *z*, to get:

$$\Gamma = \Gamma_{E1-E1} + \frac{1}{2} k E_0 E_0' \sin(2kz) \left(\frac{\omega}{3} (A''_{xxz} + A''_{yyz}) - G'_{xy} + G'_{yx} \right). \tag{6.27}$$

6.3.5 Experiment to detect achiral multipole transitions

We propose a conceptually simple experiment to probe the achiral multipole transitions of molecules at a liquid interface. A transparent slab of thickness $(n/2 + ¼)\lambda$, where n is an integer, is immersed in a liquid. The liquid molecules near the surface are oriented by interaction with the slab, so the orientation is in the opposite sense on the two faces. A standing wave is generated perpendicular to the slab. The absorption is monitored, for instance by fluorescence, as the standing wave is translated along the optic axis (Fig. 6.2).

The total fluorescence from the bulk is independent of the position of the standing wave. If there is an enrichment or depletion of molecules near the surfaces of the slab, the periodic modulation in the E1-E1 fluorescence from one face is cancelled by an out-of-phase modulation in the E1-E1 fluorescence from the opposite face (a consequence of the choice of slab thickness). But if the molecules are oriented by interaction with the faces of the slab, then both the orientation and the direction of the electric field gradient are opposite on the two faces. The achiral multipole transitions from the two phases thereby have *in phase* periodic modulation. One records the total fluorescence as a function of time, and the amplitude of the oscillatory component indicates the strength of these transitions. One can also conceive a variant of this experiment in which the liquid forms a thin film in a channel of thickness $(n/2 + ¼)\lambda$.

6.3.6 Multipole transitions in circularly polarized standing waves

Standing waves with circular polarization also excite certain multipole transitions with greater selectivity than is obtained from circularly polarized plane waves. Consider a standing wave consisting of counterpropagating left- and right-circularly polarized waves, with possibly different amplitudes:

$$\tilde{\mathbf{E}}(z,t) = \frac{E_0}{\sqrt{2}}\left(\hat{\mathbf{e}}_x + i\hat{\mathbf{e}}_y\right)\exp\left(i(kz-\omega t)\right) - \frac{E_0'}{\sqrt{2}}\left(\hat{\mathbf{e}}_x + i\hat{\mathbf{e}}_y\right)\exp\left(i(-kz-\omega t)\right).$$

$$\tilde{\mathbf{B}}(z,t) = \frac{E_0}{c\sqrt{2}}\left(\hat{\mathbf{e}}_y - i\hat{\mathbf{e}}_x\right)\exp\left(i(kz-\omega t)\right) + \frac{E_0'}{c\sqrt{2}}\left(\hat{\mathbf{e}}_y - i\hat{\mathbf{e}}_x\right)\exp\left(i(-kz-\omega t)\right). \tag{6.28}$$

We call this the $\sigma^+\sigma^-$ configuration. The standing wave generates the following EM quantities which couple to multipole transitions:

E1-E1: $$\omega\left\langle |\mathbf{E}|^2 \right\rangle_t = \frac{\omega}{2}\left[E_0^2 + E_0'^2 - 2E_0E_0'\cos(2kz)\right] \tag{6.29}$$

Chiral E1-E2: $$\frac{2\omega}{3} < E_xE_{yz} >_t = -\frac{2\omega}{3} < E_yE_{xz} >_t = -\frac{\omega k}{6}(E_0^2 - E_0'^2) \tag{6.30}$$

Achiral E1-E2: $$\frac{2\omega}{3} < E_xE_{xz} >_t = \frac{2\omega}{3} < E_yE_{yz} >_t = \frac{\omega k}{3}\sin(2kz)E_0E_0' \tag{6.31}$$

Achiral E1-M1: $$< E_x\dot{B}_y - \dot{E}_xB_y >_t = - < E_y\dot{B}_x - \dot{E}_yB_x >= -kE_0E_0'\sin(2kz) \tag{6.32}$$

Chiral E1-M1: $$< E_x\dot{B}_x - \dot{E}_xB_x >_t = < E_y\dot{B}_y - \dot{E}_yB_y >_t = -\frac{(E_0^2 - E_0'^2)k}{2}. \tag{6.33}$$

As we found with linear polarization, the achiral E1-E2 and E1-M1 transitions are not excited by a single plane wave (setting E_0 or E_0' to zero), but are only found in the standing wave. These transitions are truly invisible to plane-wave spectroscopy.

We refer to terms containing $E_x E_{yz}$ and $E_y E_{xz}$ as chiral, because these are responsible for optical activity of oriented chiral molecules. Our group previously showed that there exist configurations of the EM field in which the ratio of optical chirality to electric energy density is enhanced relative to the ratio found in circularly polarized light (CPL)[95]. It is then interesting to ask whether the same fields show an enhancement in the relative strength of the chiral E1-E2 terms.

The chiral selectivity of a light-matter interaction is described by the dissymmetry factor, defined as the fractional difference in rate of excitation between two mirror-image configurations of the fields (or the molecule).

$$g \equiv \frac{2\left(\Gamma^{+} - \Gamma^{-}\right)}{\left(\Gamma^{+} + \Gamma^{-}\right)}. \tag{6.34}$$

We previously considered isotropic chiral molecules for which the only chiral transition is E1-M1. We found that in a near-node of a $\sigma^{+}\sigma^{-}$ standing wave,

$$g_{\max} = g_{CPL} \frac{E_0 + E_0'}{E_0 - E_0'}. \tag{6.35}$$

As $E_0 \to E_0'$, this enhancement factor can become very large.

Comparison of Eqs. 6.30 and 6.33 shows that both equations have the same dependence on E_0 and E_0' and that both equations are independent of position. Thus the

dissymmetry factor for E1-E2 transitions in oriented chiral molecules in a $\sigma^+\sigma^-$ standing wave undergoes the same enhancement as for E1-M1 transitions in unoriented molecules. In this regard, the fields in regions near the electric minima are truly "superchiral" for the $\sigma^+\sigma^-$ configuration.

6.4 Magnetic Circular Dichroism

Just as the optical chirality, *C* determines the local strength of circular dichroism, we expect another EM quantity, Ξ, to determine the local strength of magnetic CD (MCD). While *C* is a time-even pseudo-scalar, we expect Ξ to be a time-odd axial vector.

MCD arises through a magnetic modification to the electric dipole polarizability tensor[87,102]. In the presence of a DC magnetic field, the electric field-induced dipole moment becomes:

$$\begin{aligned}\tilde{\mu}_\alpha &= \tilde{\alpha}_{\alpha\beta\gamma}\tilde{E}_\beta B_\gamma \\ &= (\alpha'_{\alpha\beta\gamma} + i\alpha''_{\alpha\beta\gamma})(E_\beta + \frac{i}{\omega}\dot{E}_\beta)B_\gamma\end{aligned}, \tag{6.36}$$

where $\tilde{\alpha}_{\alpha\beta\gamma}$ is the perturbation to the electric polarizability tensor by the static external field B_γ. The term proportional to $\alpha'_{\alpha\beta\gamma}$ is responsible for MCD [99]. The rate of absorption is

$$E_\alpha \dot{\mu}_\alpha = \alpha'_{\alpha\beta\gamma} E_\alpha \dot{E}_\beta B_\gamma . \tag{6.37}$$

As with regular absorption, MCD arises through a purely E1-E1 transition, in the sense that only the oscillating electric fields of the incident light need to be considered. The static magnetic field cannot contribute to absorption. However, the tensor $\tilde{\alpha}_{\alpha\beta\gamma}$ contains

an antisymmetric component with respect to exchange of the first two indices, in contrast to the usual polarizability $\tilde{\alpha}_{\alpha\beta}$ which is symmetric. This antisymmetry explains why the real part of $\tilde{\alpha}_{\alpha\beta\gamma}$ determines MCD, while the imaginary part of $\tilde{\alpha}_{\alpha\beta}$ determines regular absorption.

If we consider randomly oriented molecules, then the relevant isotropically averaged field quantity is:

$$\varepsilon_{\alpha\beta\gamma} E_\alpha \dot{E}_\beta B_\gamma = (\mathbf{E} \times \dot{\mathbf{E}}) \cdot \mathbf{B} . \tag{6.38}$$

Eq. 6.6.38 implies that $\Xi = \mathbf{E} \times \dot{\mathbf{E}}$ is the quantity that couples to MCD. This quantity is maximized when **E** and $\dot{\mathbf{E}}$ are orthogonal, i.e. when the electric field describes a circle. The optical-frequency magnetic field and electric and magnetic gradients are irrelevant for MCD. Thus MCD is maximized for circularly polarized light, and we do not expect to find sculpted fields with enhanced MCD. This finding contrasts with the enhancements predicted for chiral CD, and highlights the different physical origins of these two effects.

The expression for Ξ captures the physical picture of the electric field vector rotating about an axis, which is often associated with circular polarization. However, circular polarization is not necessary for **E** to describe a circle. Consider a Gaussian beam coming to a focus, with linear polarization in *x*, propagating in *z*. The electric field is given by the well-known expression[103].

$$E_x = E_0 \frac{w_0}{w(z)} \exp\left(\frac{-r^2}{w^2(z)} - ikz - ik \frac{r^2}{2z\left(1+\left(\frac{z_R}{z}\right)^2\right)} + i \arctan\left(\frac{z}{z_R}\right) \right), \tag{6.39}$$

where w_0 is the beam waist, $z_R = \frac{\pi w_0^2}{\lambda}$ is the Rayleigh range, and $w(z) = w_0 \sqrt{1+\left(\frac{z}{z_R}\right)^2}$.

There is also a component of the electric field along *z*. To first order in $\frac{\lambda}{w_0}$, E_z is [104]:

$$E_z = \frac{i}{k} \frac{\partial E_x}{\partial x}. \tag{6.40}$$

Near the focus, the electric field rotates in the x-z plane, which generates a non-zero time average of $\mathbf{E} \times \dot{\mathbf{E}}$. At the beam waist, *z* = 0, we find:

$$\left\langle \mathbf{E} \times \dot{\mathbf{E}} \right\rangle_t = \left(0, \frac{-2\omega E_0^2 x}{k w_0^2} \exp\left(\frac{-2r^2}{{w_0}^2} \right), 0 \right). \tag{6.41}$$

Therefore we predict that a DC magnetic field in the $\hat{y}$ direction gives rise to differential absorption across the beam cross section. This signal has the same origin as magnetic CD.

We propose an experiment to demonstrate this effect via fluorescence detected MCD (FDMCD), as illustrated in Fig. 6.3. A thin film of fluorescent material is placed in the focus of a linearly polarized beam. An external magnetic field is applied transverse to the beam and the polarization. The small FDMCD signal is superimposed on the much larger E1-E1 fluorescence, so the FDMCD appears as a slight shift along the *x*-axis of the

peak position of the fluorescence. By modulating the magnetic field, this peak is made to oscillate along *x*, leading to a fluorescence signal that can be detected with a spatially resolved detector and a lock-in amplifier.

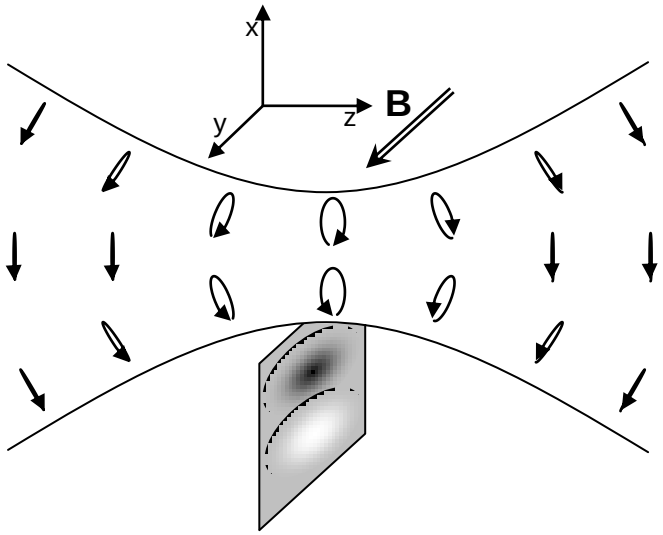

Figure 6.3. Magnetic circular dichroism in a focused linearly polarized beam. Near the focus, the electric field describes an ellipse in the *x*-*z* plane. A magnetic field along the *y* axis is predicted to induce a differential absorption across the beam.

6.5 Relation to the Lipkin Zilch

In 1964 Lipkin introduced ten new conserved electromagnetic quantities, but did not find a physical interpretation [96]. We recently showed that one of these terms, Z^{000} is the same as our optical chirality, *C* [95]. Here we show that the remaining nine terms are linear combinations of quantities that we derived above.

Consider six of Lipkin's terms given by the off-diagonal elements of

$$Z^{\alpha\beta 0} \equiv \delta_{\alpha\beta}[\mathbf{E}\cdot\nabla\times\mathbf{E}+\mathbf{H}\cdot\nabla\times\mathbf{H}]-E_\alpha(\nabla\times\mathbf{E})_\beta-E_\beta(\nabla\times\mathbf{E})_\alpha-H_\alpha(\nabla\times\mathbf{H})_\beta-H_\beta(\nabla\times\mathbf{H})_\alpha$$

. (6.42)

The three off-diagonal terms in $Z^{\alpha\beta 0}$ each separate into two terms of the form

$$-E_\alpha(\nabla\times\mathbf{E})_\beta - H_\beta(\nabla\times\mathbf{H})_\alpha . \tag{6.43}$$

Using Gaussian units with $c = 1$ as used in Lipkin's paper, and applying Maxwell's equations in free space, we have

$$E_\alpha\dot{B}_\beta - \dot{E}_\alpha B_\beta \rightarrow -E_\alpha(\nabla\times\mathbf{E})_\beta - H_\beta(\nabla\times\mathbf{H})_\alpha . \tag{6.44}$$

Therefore each off-diagonal element $Z^{\alpha\beta 0}$ is a linear combination of the EM quantities that drive E1-M1 transitions.

There are three additional conserved quantities from Lipkin of the form:

$$(\mathbf{E}\times\dot{\mathbf{E}} + \mathbf{H}\times\dot{\mathbf{H}})_\alpha . \tag{6.45}$$

These are components of the flux of optical chirality *C*, and are also related to MCD. We showed above that the quantity $\mathbf{E}\times\dot{\mathbf{E}}$ determines the extent of MCD. If we also consider the perturbation to the magnetic polarizability by a magnetic field, then an identical procedure would identify $\mathbf{H}\times\dot{\mathbf{H}}$ as the relevant quantity for magnetic dipole transitions. Magnetic dipole transitions are normally much weaker than electric dipole transitions, and can be neglected.

Conservation in vacuum for each of the Lipkin terms is a special case of a general conservation law for any quantity of the form:

$$Y = A\dot{B} - B\dot{A}, \tag{6.46}$$

where *A* and *B* are components of **E** and **B** acted on by any linear operator, such as time or spatial derivative. We define the corresponding flux

$$\mathbf{\Phi} \equiv -A\nabla B + B\nabla A\,, \tag{6.47}$$

and immediately obtain a conservation law in free space:

$$\dot{Y} + \nabla \cdot \mathbf{\Phi} = 0\,, \tag{6.488}$$

This procedure gives an infinite number of quantities that are conserved in vacuum. These quantities are likely to have the physical interpretation of being the couplings to molecular polarizability tensor components.

6.6 Discussion

We showed that there exist many configurations of the electromagnetic fields and field gradients that cannot be generated from a single plane wave; but that *any* local configuration of the field can be generated from a combination of plane waves. There exist achiral multipole transitions in oriented molecules that are completely invisible to plane waves, but that are detectable in suitably designed optical standing waves. Just as circular dichroism measurements probe aspects of molecular structure that are not detected by conventional absorption, we expect these achiral multipole transitions also to hold new molecular information. We also found that a tightly focused beam of linearly polarized light in a magnetic field probes the molecular properties usually probed by magnetic circular dichroism. Here we considered only linear optics, where the rate of excitation is quadratic in the fields. The field objects we considered here can appear in greater number when one considers nonlinear optics, and interesting effects may arise in that domain as well.[105]

Appendix 1: Plane-wave basis for local field geometries

At a single point in space, one requires sixteen independent complex quantities to describe the electric field, magnetic field, electric gradients and magnetic gradients for a time-harmonic solution to Maxwell's Equations. These quantities can be arranged in a sixteen-dimensional vector $\tilde{\mathbf{Q}}\exp(-i\omega t)$, where $\tilde{\mathbf{Q}}$ is complex. We choose to construct a basis for $\tilde{\mathbf{Q}}$ from plane waves of the form $\mathbf{E}^{(0)}\exp(i\mathbf{k}\cdot\mathbf{r}-i\omega t)\exp(i\phi)$, for which we can choose the phase ϕ to give the real and imaginary parts independently. Therefore it is sufficient to show that one can construct the real part of $\tilde{\mathbf{Q}}$ from plane waves. The imaginary part follows similarly.

In the following table, we list 16 plane waves and their associated vectors in the space of $\tilde{\mathbf{Q}}$, calculated at the origin **r** = 0. A similar set with $\phi = \pi/2$ completes the basis for all possible EM fields and gradients at **r** = 0. These vectors can be verified to be linearly independent by checking that the determinant of the 16 by 16 matrix is non-zero. Therefore these vectors form a basis for the vector space. Of course this choice of basis is not unique. We have chosen units of time and distance such that $k_0 = c = 1$. We only give five of the gradients of **E** and **B**; the others are determined from Maxwell's Equations.

TABLE A1. Sixteen plane waves with phase $\phi = 0$, which span the real part of the space of possible electromagnetic fields and field gradients.

k	**E**	**B**	$(E_{xy}, E_{yz}, E_{zx}, E_{xx}, E_{yy})$	$(B_{xy}, B_{yz}, B_{zx}, B_{xx}, B_{yy})$
(0, 1,0)	$(E_1,0,0)$	$(0,0,-E_1)$	$(E_1,0,0,0,0)$	(0,0,0,0,0)
(0, 0,1)	$(E_2,0,0)$	$(0,E_2,0)$	(0,0,0,0,0)	$(0,E_2,0,0,0)$
(1,0,0)	$(0,E_3,0)$	$(0,0,E_3)$	(0,0,0,0,0)	$(0,0,E_3,0,0)$
(0, 0,1)	$(0,E_4,0)$	$(-E_4,0,0)$	$(0,E_4,0,0,0)$	(0,0,0,0,0)
(1,0,0)	$(0,0,E_5)$	$(0,-E_5,0)$	$(0,0,E_5,0,0)$	(0,0,0,0,0)
(0, 1,0)	$(0,0,E_6)$	$(E_6,0,0)$	(0,0,0,0,0)	$(E_6,0,0,0,0)$
(0, 0,-1)	$(E_7,0,0)$	$(0,-E_7,0)$	(0,0,0,0,0)	$(0,E_7,0,0,0)$
(-1,0,0)	$(0,E_8,0)$	$(0,0,-E_8)$	(0,0,0,0,0)	$(0,0,E_8,0,0)$
(0, -1,0)	$(0,0,E_9)$	$(-E_9,0,0)$	(0,0,0,0,0)	$(E_9,0,0,0,0)$
$(\frac{1}{\sqrt{2}},0,-\frac{1}{\sqrt{2}})$	$(E_{10},0,E_{10})$	$(0,-\sqrt{2}E_{10},0)$	$(0,0,\frac{E_{10}}{\sqrt{2}},\frac{E_{10}}{\sqrt{2}},0)$	$(0,E_{10},0,0,0)$
$(0,\frac{1}{\sqrt{2}},-\frac{1}{\sqrt{2}})$	$(0,E_{11},E_{11})$	$(\sqrt{2}E_{11},0,0)$	$(0,\frac{-E_{11}}{\sqrt{2}},0,0,\frac{E_{11}}{\sqrt{2}})$	$(E_{11},0,0,0,0)$
(0, -1,0)	$(E_{12},0,0)$	$(0,0,E_{12})$	$(-E_{12},0,0,0,0)$	(0,0,0,0,0)
(0, 0,-1)	$(0,E_{13},0)$	$(E_{13},0,0)$	$(0,-E_{13},0,0,0)$	(0,0,0,0,0)
(-1,0,0)	$(0,0,E_{14})$	$(0,E_{14},0)$	$(0,0,-E_{14},0,0)$	(0,0,0,0,0)
$(\frac{1}{\sqrt{2}},0,-\frac{1}{\sqrt{2}})$	$(0,E_{15},0)$	$(\frac{E_{15}}{\sqrt{2}},0,\frac{E_{15}}{\sqrt{2}})$	$(0,\frac{-E_{15}}{\sqrt{2}},0,0,0)$	$(0,0,\frac{E_{15}}{2},\frac{E_{15}}{2},0)$
$(0,\frac{1}{\sqrt{2}},-\frac{1}{\sqrt{2}})$	$(E_{16},0,0)$	$(0,\frac{-E_{16}}{\sqrt{2}},\frac{-E_{16}}{\sqrt{2}})$	$(\frac{E_{16}}{\sqrt{2}},0,0,0,0)$	$(0,\frac{E_{16}}{2},0,0,\frac{-E_{16}}{2})$

References

1. N. Yang, Y. Tang, and A. E. Cohen, "Spectroscopy in sculpted fields," Nano Today **4,** 269-279 (2009).

2. U. E. Steiner and T. Ulrich, "Magnetic field effects in chemical kinetics and related phenomena," Chem. Rev. **89,** 51-147 (1989).

3. N. J. Turro, "Influence of nuclear spin on chemical reactions: magnetic isotope and magnetic field effects (a review)," Proc. Nat. Acad. Sci. U. S. A. **80,** 609-621 (1983).

4. S. Nagakura, H. Hayashi, and T. Azumi, *Dynamic Spin Chemistry: Magnetic Controls and Spin Dynamics of Chemical Reactions* (Wiley-Kodansha, 1998).

5. H. Hayashi, *Introduction to dynamic spin chemistry* (World Scientific, 2004).

6. R. Kaptein and J. Oosterhoff, "Chemically induced dynamic nuclear polarization II:(Relation with anomalous ESR spectra)," Chemical Physics Letters **4,** 195-197 (1969).

7. R. Kaptein and L. J. Oosterhoff, "Chemically induced dynamic nuclear polarization III (anomalous multiplets of radical coupling and disproportionation products)," Chemical Physics Letters **4,** 214-216 (1969).

8. G. L. Closs, "Mechanism explaining nuclear spin polarizations in radical combination reactions," J. Am. Chem. Soc. **91,** 4552-4554 (1969).

9. R. Kaptein, "Chemically induced dynamic nuclear polarization. VIII. Spin dynamics and diffusion of radical pairs," J. Am. Chem. Soc. **94,** 6251-6262 (1972).

10. J. Birks, "Excimers and exciplexes," Nature **214,** 1187-1190 (1967).

11. A. B. Zahlan, *The triplet state* (Cambridge University Press, 1967).

12. R. Kubo, "A stochastic theory of spin relaxation," Hyperfine Interactions **8,** 731-738 (1981).

13. R. Kubo and T. Toyabe, in *Magnetic Resonance and Relaxation*, R. Blinc, ed. (North-Holland, 1967), pp. 810.

14. A. E. Cohen, "Nanomagnetic Control of Intersystem Crossing," J Phys Chem A **113,** 11084-11092 (2009).

15. C. Timmel, U. Till, B. Brocklehurst, K. McLauchlan, and P. Hore, "Effects of weak magnetic fields on free radical recombination reactions," Mol. Phys. **95,** 71-89 (1998).

16. C. R. Timmel and K. B. Henbest, "A study of spin chemistry in weak magnetic fields," Phil. Trans. A **362,** 2573 (2004).

17. P. W. Atkins and T. P. Lambert, "Chapter 4. The effect of a magnetic field on chemical reactions," Annual Reports on the Progress of Chemistry, Section A: Physical and Inorganic Chemistry **72,** 67-88 (1975).

18. C. T. Rodgers, "Magnetic field effects in chemical systems," Pure and Applied Chemistry **81,** 19 (2009).

19. A. Weller, F. Nolting, and H. Staerk, "A quantitative interpretation of the magnetic-field effect on hyperfine-coupling-induced triplet formation from radical ion-pairs," Chem. Phys. Lett. **96,** 24-27 (1983).

20. P. Kumar Bera, D. Nath, A. Misra, and M. Chowdhury, "A comparative study of two exciplexes: anthracene-dimethylaniline and anthracene-julolidine systems," J. Photochem. Photobiol. A. **95,** 127-136 (1996).

21. T. Sengupta and S. Basu, "Magnetic field effect on indole exciplexes: a comparative study," Spectrochimica Acta Part A: Molecular and Biomolecular Spectroscopy **60,** 1127-1132 (2004).

22. N. K. Petrov, A. I. Shushin, and E. L. Frankevich, "Solvent effect on magnetic field modulation of exciplex fluorescence in polar solutions," Chemical Physics Letters **82,** 339-343 (1981).

23. D. N. Nath and M. Chowdhury, "Effect of variation of dielectric constant on the magnetic field modulation of exciplex luminescence," Pramana **34,** 51-66 (1990).

24. H. J. Werner, H. Staerk, and A. Weller, "Solvent, isotope, and magnetic-field effects in geminate recombination of radical ion-pairs," J. Chem. Phys. **68,** 2419-2426 (1978).

25. H. Staerk, W. Kuhnle, R. Treichel, and A. Weller, "Magnetic-field dependence of intramolecular exciplex formation in polymethylene-linked A-D systems," Chem. Phys. Lett. **118,** 19-24 (1985).

26. Y. Tanimoto, N. Okada, and M. Itoh Kaoru, "Magnetic field effects on the fluorescence of intramolecular electron-donor-acceptor systems," Chemical Physics Letters **136,** 42-46 (1987).

27. S. Basu, D. Nath, M. Chowdhury, and M. A. Winnik, "Magnetic field effects in a polymer-chain-linked donor-acceptor system," Chem. Phys. **162,** 145-153 (1992).

28. H. Cao, Y. Fujiwara, T. Haino, Y. Fukazawa, C. H. Tung, and Y. Tanimoto, "Magnetic Field Effects on Intramolecular Exciplex Fluorescence of Chain-Linked Phenanthrene and N, N-Dimethylaniline: Influence of Chain Length, Solvent, and Temperature," Bull. Chem. Soc. Jpn. **69,** 2801-2813 (1996).

29. H. Cao, K. Miyata, T. Tamura, Y. Fujiwara, A. Katsuki, C. H. Tung, and Y. Tanimoto, "Effects of high magnetic field on the intramolecular exciplex fluorescence of chain-linked phenanthrene and dimethylaniline," J Phys Chem A **101,** 407-411 (1997).

30. C. D. Borsarelli, J. J. Cosa, and C. M. Previtali, "Exciplex formation between pyrene derivatives and N, N-dimethylaniline in aerosol OT reversed micelles," Langmuir **8,** 1070-1075 (1992).

31. F. L. Cozens and J. C. Scaiano, "A Comparative-Study of Magnetic-Field Effects on the Dynamics of Geminate and Random Radical Pair Processes in Micelles," J. Am. Chem. Soc. **115,** 5204-5211 (1993).

32. K. Bhattacharyya and M. Chowdhury, "Environmental and magnetic field effects on exciplex and twisted charge transfer emission," Chem. Rev. **93,** 507-535 (1993).

33. F. Nolting, H. Staerk, and A. Weller, "Magnetic field effect on the hyperfine-induced triplet formation in systems undergoing donor to radical pair electron transfer," Chemical Physics Letters **88,** 523-527 (1982).

34. A. Buchachenko, E. Galimov, V. Ershov, G. Nikiforov, and A. Pershin,"Isotopic enrichment induced by magnetic-interactions in chemical-reactions" in *Dokl. Akad. Nauk SSSR*Anonymous , 1976).

35. N. J. Turro and G. C. Weed, "Micellar systems as supercages for reactions of geminate radical pairs. Magnetic effects," J. Am. Chem. Soc. **105,** 1861-1868 (1983).

36. J. Bargon, H. Fischer, and U. Johnsen, "Kernresonanz-Emissionslinien während rascher Radikalreaktionen. I. Aufnahmeverfahren und Beispiele," Zeitschrift Naturforschung Teil A **22,** 1551 (1967).

37. H. R. Ward and R. G. Lawler, "Nuclear magnetic resonance emission and enhanced absorption in rapid organometallic reactions," J. Am. Chem. Soc. **89,** 5518-5519 (1967).

38. R. Kaptein, K. Dijkstra, and K. Nicolay, "Laser photo-CIDNP as a surface probe for proteins in solution," Nature **274,** 293-294 (1978).

39. R. Kaptein, "Photo-CIDNP studies of proteins," Biological magnetic resonance **4,** 145-191 (1982).

40. P. Hore, C. Joslin, and K. Mclauchan, "Chemically induced dynamic electron polarization," J.Chem.Soc.Spec.Period.Rep.ESR **5,** 1-45 (1979).

41. A. R. Lepley and G. Closs, *Chemically induced magnetic polarization* (Wiley New York, 1973).

42. C. I. M. Polarization, "Muus, LT, Atkins, PW, McLauchlan, KA, Pedersen, JB, Eds," D.Reidel: Dordrecht, The Netherlands (1977).

43. O. Anisimov, V. Grigoryants, V. Molchanov, and Y. N. Molin, "Optical detection of ESR absorption of short-lived ion-radical pairs produced in solution by ionizing radiation," Chemical Physics Letters **66,** 265-268 (1979).

44. Y. N. Molin, O. Anisimov, V. Grigor'yants, V. Molchanov, and K. Salikhov, "Optical detection of ESR spectra of short-lived ion-radical pairs produced in solution by ionizing radiation," J. Phys. Chem. **84,** 1853-1856 (1980).

45. M. Okazaki and T. Shiga, "Product yield of magnetic-field-dependent photochemical reaction modulated by electron spin resonance," (1986).

46. K. Enjo, K. Maeda, H. Murai, T. Azumi, and Y. Tanimoto, "Reaction-yield-detected magnetic resonance in the intra-and intermolecular electron transfer reactions," Applied Magnetic Resonance **12,** 423-430 (1997).

47. A. L. Buchachenko and V. L. Berdinsky, "Electron spin catalysis," Chem. Rev. **102,** 603-612 (2002).

48. E. N. Step, A. L. Buchachenko, and N. J. Turro, "Paramagnetic Interactions of Triplet Radical Pairs with Nitroxide Radicals: An" Antiscavenging" Effect," J. Am. Chem. Soc. **116,** 5462-5466 (1994).

49. P. Atkins and M. Clugston, "Ortho-para hydrogen conversion in paramagnetic solutions," Mol. Phys. **27,** 1619-1631 (1974).

50. K. G. Petzinger and D. J. Scalapino, "Para- to Ortho-Hydrogen Conversion on Magnetic Surfaces," Phys. Rev. B **8,** 266-279 (1973).

51. W. Wiltschko and R. Wiltschko, "Magnetic orientation and magnetoreception in birds and other animals," Journal of Comparative Physiology A: Neuroethology, Sensory, Neural, and Behavioral Physiology **191,** 675-693 (2005).

52. S. Johnsen and K. J. Lohmann, "The physics and neurobiology of magnetoreception," Nature reviews neuroscience **6,** 703-712 (2005).

53. S. Johnsen and K. J. Lohmann, "Magnetoreception in animals," Phys Today **61,** 29 (2008).

54. T. Ritz, S. Adem, and K. Schulten, "A Model for Photoreceptor-Based Magnetoreception in Birds," Biophys. J. **78,** 707-718 (2000).

55. K. Schulten, C. E. Swenberg, and A. Weller, "A biomagnetic sensory mechanism based on magnetic field modulated coherent electron spin motion," Zeitschrift für Physikalische Chemie **111,** 1-5 (1978).

56. K. Maeda, K. B. Henbest, F. Cintolesi, I. Kuprov, C. T. Rodgers, P. A. Liddell, D. Gust, C. R. Timmel, and P. J. Hore, "Chemical compass model of avian magnetoreception," Nature **453,** 387-390 (2008).

57. W. Wiltschko, U. Munro, H. Ford, and R. Wiltschko, "Red light disrupts magnetic orientation of migratory birds," (1993).

58. W. Wiltschko and R. Wiltschko, "Light-dependent magnetoreception in birds: the behaviour of European robins, Erithacus rubecula, under monochromatic light of various wavelengths and intensities," J. Exp. Biol. **204,** 3295-3302 (2001).

59. W. Wiltschko and R. Wiltschko, "Magnetic compass of European robins," Science **176,** 62-64 (1972).

60. T. Ritz, P. Thalau, J. B. Phillips, R. Wiltschko, and W. Wiltschko, "Resonance effects indicate a radical-pair mechanism for avian magnetic compass," Nature **429,** 177-180 (2004).

61. R. J. Gegear, A. Casselman, S. Waddell, and S. M. Reppert, "Cryptochrome mediates light-dependent magnetosensitivity in Drosophila," Nature **454,** 1014 (2008).

62. C. T. Rodgers and P. J. Hore, "Chemical magnetoreception in birds: The radical pair mechanism," Proc. Nat. Acad. Sci. U. S. A. **106,** 353-360 (2009).

63. H. Mouritsen, U. Janssen-Bienhold, M. Liedvogel, G. Feenders, J. Stalleicken, P. Dirks, and R. Weiler, "Cryptochromes and neuronal-activity markers colocalize in the retina of migratory birds during magnetic orientation," Proc. Natl. Acad. Sci. U. S. A. **101,** 14294-14299 (2004).

64. L. Q. Wu and J. D. Dickman, "Neural correlates of a magnetic sense," Science Signalling **336,** 1054 (2012).

65. R. Haberkorn and M. Michel-Beyerle, "On the mechanism of magnetic field effects in bacterial photosynthesis," Biophys. J. **26,** 489-498 (1979).

66. R. E. Blankenship, T. J. Schaafsma, and W. W. Parson, "Magnetic field effects on radical pair intermediates in bacterial photosynthesis," Biochim. Biophys. Acta **461,** 297 (1977).

67. A. L. Buchachenko, D. A. Kouznetsov, M. A. Orlova, and A. A. Markarian, "Magnetic isotope effect of magnesium in phosphoglycerate kinase phosphorylation," Proc. Natl. Acad. Sci. U. S. A. **102,** 10793-10796 (2005).

68. M. J. Crumpton, "The Bernal Lecture 2004 Are low-frequency electromagnetic fields a health hazard?" Philosophical Transactions of the Royal Society B: Biological Sciences **360,** 1223-1230 (2005).

69. P. Hore, "Are biochemical reactions affected by weak magnetic fields?" Proceedings of the National Academy of Sciences **109,** 1357-1358 (2012).

70. I. B. Berlman Handbook of fluorescence spectra of aromatic molecules (1971).

71. K. Kalyanasundaram and J. Thomas, "Environmental effects on vibronic band intensities in pyrene monomer fluorescence and their application in studies of micellar systems," J. Am. Chem. Soc. **99,** 2039-2044 (1977).

72. A. Weller, H. Staerk, and R. Treichel, "Magnetic-field effects on geminate radical-pair recombination," Faraday Discuss. Chem. Soc. **78,** 271-278 (1984).

73. H. J. Werner, Z. Schulten, and K. Schulten, "Theory of the magnetic field modulated geminate recombination of radical ion pairs in polar solvents: application to the pyrene–N, N-dimethylaniline system," J. Chem. Phys. **67,** 646 (1977).

74. K. Schulten and P. G. Wolynes, "Semiclassical description of electron spin motion in radicals including the effect of electron hopping," J. Chem. Phys. **68,** 3292 (1978).

75. N. K. Petrov, V. N. Borisenko, A. V. Starostin, and M. V. Alfimov, "Polar Molecular Clusters Produced upon Photoinduced Electron Transfer in an Intermolecular Exciplex in Binary Solvents," J. Phys. Chem. **96,** 2901 (1992).

76. D. R. Kattnig, A. Rosspeintner, and G. Grampp, "Fully Reversible Interconversion between Locally Excited Fluorophore, Exciplex, and Radical Ion Pair Demonstrated by a New Magnetic Field Effect," Angewandte Chemie International Edition **47,** 960-962 (2007).

77. B. Hu, L. Yan, and M. Shao, "Magnetic-Field Effects in Organic Semiconducting Materials and Devices," Adv. Mater. **21,** 1500 (2009).

78. N. Yang and A. E. Cohen, "Optical imaging through scattering media via magnetically modulated fluorescence," Opt. Express **18,** 25461 (2010).

79. Z. Yaqoob, D. Psaltis, M. S. Feld, and C. Yang, "Optical phase conjugation for turbidity suppression in biological samples," Nature photonics **2,** 110-115 (2008).

80. I. M. Vellekoop and C. M. Aegerter, "Scattered light fluorescence microscopy: imaging through turbid layers," Opt. Lett. **35,** 1245-1247 (2010).

81. D. Huang, E. A. Swanson, C. P. Lin, J. S. Schuman, W. G. Stinson, W. Chang, M. R. Hee, T. Flotte, K. Gregory, C. A. Puliafito, and J. G. Fujimoto, "Optical coherence tomography," Science **254,** 1178-1181 (1991).

82. H. F. Zhang, K. Maslov, G. Stoica, and L. V. Wang, "Functional photoacoustic microscopy for high-resolution and noninvasive in vivo imaging," Nat. Biotechnol. **24,** 848-851 (2006).

83. N. Y. Yang and A. E. Cohen, "Local geometry of electromagnetic fields and its role in molecular multipole transitions," J. Phys. Chem. B **115,** 5304-5311 (2011).

84. B. P. Krueger, G. D. Scholes, and G. R. Fleming, "Calculation of couplings and energy-transfer pathways between the pigments of LH2 by the ab initio transition density cube method," J. Phys. Chem. B **102,** 5378-5386 (1998).

85. U. Harbola and S. Mukamel, "Intermolecular forces and nonbonded interactions: Superoperator nonlinear time-dependent density-functional-theory response approach," Phys. Rev. A **70,** 52506 (2004).

86. J. Hachmann, J. J. Dorando, M. Aviles, and G. K. Chan, "The radical character of the acenes: a density matrix renormalization group study," J. Chem. Phys. **127,** 134309 (2007).

87. D. P. Craig and T. Thirunamachandran, *Molecular Quantum Electrodynamics* (Courier Dover Publications, 1998).

88. Akbar Salam, "
Molecular Quantum Electrodynamics: Long-Range Intermolecular Interactions," in , Anonymous (Wiley, 2009).

89. M. Moskovits, "Surface-enhanced spectroscopy," Rev. Mod. Phys. **57,** 783-826 (1985).

90. A. Nitzan and L. E. Brus, "Theoretical model for enhanced photochemistry on rough surfaces," J. Chem. Phys. **75,** 2205 (1981).

91. T. Liebermann and W. Knoll, "Surface-plasmon field-enhanced fluorescence spectroscopy," Colloids Surf. A **171,** 115-130 (2000).

92. C. L. Haynes and R. P. Van Duyne, "Plasmon-sampled surface-enhanced Raman excitation spectroscopy," J. Phys. Chem. B **107,** 7426 (2003).

93. E. J. Sánchez, L. Novotny, and X. S. Xie, "Near-Field Fluorescence Microscopy Based on Two-Photon Excitation with Metal Tips," Phys. Rev. Lett. **82,** 4014-4017 (1999).

94. A. Sundaramurthy, P. J. Schuck, N. R. Conley, D. P. Fromm, G. S. Kino, and W. E. Moerner, "Toward nanometer-scale optical photolithography: utilizing the near-field of bowtie optical nanoantennas," Nano Lett. **6,** 355-360 (2006).

95. Y. Tang and A. E. Cohen, "Optical chirality and its Interaction with matter," Phys. Rev. Lett. **104,** 163901 (2010).

96. D. M. Lipkin, "Existence of a new conservation law in electromagnetic theory," J. Math. Phys. **5,** 696 (1964).

97. D. J. Candlin, "Analysis of the new conservation law in electromagnetic theory," Il Nuovo Cimento **37,** 1390-1395 (1965).

98. T. W. B. Kibble, "Conservation laws for free fields," J. Math. Phys. **6,** 1022 (1965).

99. L. D. Barron, *Molecular Light Scattering and Optical Activity* (Cambridge University Press, 2004).

100. P. W. Atkins and R. S. Friedman, *Molecular quantum mechanics* (Oxford university press Oxford, 1983).

101. A. Buckingham and M. Dunn, "Optical activity of oriented molecules," J. Chem. Soc. (A) **1971,** 1988-1991 (1971).

102. W. P. Healy, "The multipole Hamiltonian and magnetic circular dichroism," J. Chem. Phys. **64,** 3111 (1976).

103. A. E. Siegman, *Lasers* (University Science Books, 1986).

104. L. W. Davis, "Theory of electromagnetic beams," Physical Review A **19,** 1177-1179 (1979).

105. S. Mukamel, *Principles of Nonlinear Optical Spectroscopy* (Oxford University Press, 1995).